

# Simple Book Example

TeXstudio Team

January 2013

ii

thesis

# Contents

<b>1 Theory and methods of plenoptic imaging</b>	<b>1</b>
1.1 Introduction . . . . .	1
1.2 Plenoptic function and the light field . . . . .	3
1.3 Plenoptic camera . . . . .	6
1.4 Plenoptic Camera 1.0 . . . . .	8
1.4.1 Phase space in plenoptic 1.0 . . . . .	14
1.4.2 Light Field Parametrization . . . . .	16
1.5 Plenoptic 1.0 rendering . . . . .	21
1.6 Plenoptic Camera 2.0 . . . . .	24
1.7 Plenoptic camera 2.0: a geometrical optics analysis . . . . .	32
1.8 Plenoptic 2.0 rendering . . . . .	36
<b>2 Fresnel Simulation Toolbox</b>	<b>39</b>
2.1 Introduction . . . . .	39
2.2 Scalar Theory of diffraction . . . . .	41
2.2.1 Helmholtz equation . . . . .	44
2.2.2 Solutions of Helmholtz Equations . . . . .	45
2.2.3 The Fresnel Approximation . . . . .	46
2.3 Operator Free space propagation: Fresnel Approximation approach . . . . .	47
2.3.1 Multi-Step Fresnel propagation operator . . . . .	49
2.4 Operator Free space propagation: Angular spectrum of plane waves approach . . . . .	51
2.4.1 Angular spectrum of plane waves . . . . .	51
2.4.2 Band Limited Angular Spectrum . . . . .	55
2.4.3 Corrected Band Limited Angular Spectrum Method . .	63
2.4.4 Performances of the Angular spectrum methods . . .	65
2.5 Operator Thin Lens . . . . .	68
2.5.1 Aliasing in phase sampling . . . . .	74
2.6 Comparison between the free space propagation operators . .	76
2.6.1 Description of the system . . . . .	77

2.6.2	Image of a point source . . . . .	78
2.7	Coherence . . . . .	83
2.7.1	Temporal coherence . . . . .	84
2.7.2	Spatial Coherence . . . . .	85
2.7.3	Simulation of spatial coherence . . . . .	86
2.7.4	Simulation of temporal coherence . . . . .	92
2.8	Optimization of coherence parameters . . . . .	93
2.8.1	Optimization of Spatial Coherence . . . . .	94
2.8.2	Optimization of temporal coherence . . . . .	97
2.8.3	Coherent imaging vs incoherent imaging . . . . .	100

# List of Figures

1.1	Differences between a traditional camera and a computational camera [1]. . . . .	2
1.2	Two point representation of light field. Each ray of light is unequivocally defined by the coordinates of two points of interception. . . . .	5
1.3	Point angle representation. A ray of light is unequivocally defined by the coordinates of a point that belongs to a plane perpendicular at the optical axis z and by the angles $\theta_x$ and $\theta_y$ that it forms with the optical axis along the directions x and y. . . . .	5
1.4	Plenoptic camera and its fundamental components. The presence of the micro array allows to record the light field . . . . .	6
1.5	Top: Plenoptic camera 1.0. The main lens is focused on the object and forms and image on the micro array and the micro array. $f$ is the focal length of the main lens and $f_\mu$ the focal length of the micro lens array. Bottom: Plenoptic camera 2.0. The main lens is focused on an object and forms an image on the plane represented by the dashed line. The micro array acts as a relay between the main lens image and the sensor, since it satisfy the lens equation $1/a + 1/b = 1/f_\mu$ . . . . .	8
1.6	Ray diagram of a plenoptic 1.0 system. The main lens is in a 2f configuration and the sensor plane is conjugated with the main lens plane. The micro lens position maps the position (x,y) of the point P, while the sub image maps the directions of the rays coming from that point. The ray with direction $\theta_1$ falls on the pixel 1 (blue), the ray with direction $\theta_2$ falls on the pixel 2 (green) and the ray with direction $\theta_3$ falls on the pixel 3 (red). The sub image $d$ maps the direction of the ray.	10

1.7 Sampling of Light Filed. Each ray is described by a set of four coordinates, two spatial (x,y) and two directional (u,v). The spatial coordinates are sampled by the position of the lens let in the micro array, the directional coordinates are sampled by the pixel under the lens let. Point A, its position is sampled by the lens let number 1(x=1), and three rays are green (1,1), red(1,2), blue(1,3). Each ray is defined by x and v. Point B:for one position (x=5) three rays are sampled green (5,1), red(5,2), blue(5,3), dashed line. . . . .	12
1.8 F-number matching between the main lens and the micro lens in the array. . . . .	13
1.9 When the f-number is matched, all the rays captured by the main lens are mapped on the sub image (yellow). If the f-number is smaller (red), the sub image is smaller and there is an under sampling of the set of rays. If the f-number of the lens let is bigger (green), the sub image is larger and cross talk happens between near sub images . . . . .	14
1.10 Sampling of the light field and phase space representations of the rays. . . . .	15
1.11 Example of a raw plenoptic 1.0 image. . . . .	16
1.12 Zoom on the raw image. Each lens-let is formed by 20 X 20 pixels. Each pixel represents a direction of the rays hitting the lens let that produced the sub image. . . . .	17
1.13 The array view is an array of the different point of view obtained rearranging the pixels according to the directional coordinates. . . . .	18
1.14 The array view is an array of the different points of view obtained by rearranging the pixels according to the directional coordinates. . . . .	19
1.15 Zoom of the central part of the array view showing in detail the different points of views. . . . .	20
1.16 Sampling of the light field and phase space representations of the rays.[2] . . . . .	21
1.17 Rendering an image from plenoptic 1.0 raw data is equal to summing all the directional samples for each position. This process is shown for the the $(x, \theta_x)$ slice of the phase space. [3]	23
1.18 rendered image form the raw data in figure 1.11. Resolution is only 75 X 75 pixel. . . . .	24

1.19 If the main lens image is formed in front of the micro array the configuration is called "Copernican", top, and the focal length of the micro array is smaller then the distance b. If the main lens image is formed behind the micro array the configuration is "Galilean", on the bottom, and the focal length of the micro array is bigger then the distance b. . . . .	26
1.20 Raw data of a point source sampled by a plenoptic 2.0 system with a magnification of the micro array stage equal to 0.3. Data acquired with numerical simulations. . . . .	28
1.21 Zoomed Raw data of a point source sampled by a plenoptic 2.0 system with a magnification of the micro array stage equal to 0.3. Data acquired with numerical simulations. The grid represent the boundaries of each sub image to show how the point of view of the point source changes across the lens lets. The sub images are shifted by a quantity proportional to the position of the lens let in the array. . . . .	28
1.22 Sampling of the light field by a plenoptic 2.0 system. The one dimensional case is shown. Each micro lens has a diameter equal to $d$ , a focal length $f_\mu$ , and images the main lens image on the sensor according to the lens law $1/a + 1/b = 1/f_\mu$ . The total range of directions that can be sampled is given by $d/b$ . Each lens let samples a sub set of directions equal to $d/a$ as a single direction. The range of directions shown in red are sampled by the central micro lens as a single point of view. The angular resolution is therefore $d/a$ and the total number of directional sampled is 3. . . . .	29
1.23 Raw images of a point source simulated with different magnifications. From top left to bottom right: $m = 1$ , $m = 0.5$ , $m = 0.25$ , $m = 0.1$ . . . . .	31
1.24 System formed by a single lens let. The rays at the main lens image plane are transformed into the rays at the sensor plane by the lens let. The transformation can be described by a matrix $A$ . . . . .	34

1.25 Sampling of the light field by plenoptic 2.0 camera. For each of the two points represented, red and green, The total range of directional coordinates are sampled by three different lens lets. For one position three directions are sampled, with a resolution of $d/a$ . Therefore the directional sampling in plenoptic 2.0 is made across many lens lets. This can be seen in the phase space. Lenset B and C sample 2 directions indicated with the same number in the ray diagram and the phase space. Lens let A only samples one direction of the red point. . . . .	36
1.26 Image rendering with the focused plenoptic camera. One pixel of the rendered image is given by the integration on all the directions $d/b$ associated with a given position. The integration takes place across the lens let. . . . .	37
2.1 example . . . . .	47
2.2 To remove the scaling factor between the input and output fields, a multi step Fresnel approach has been developed. The field is propagated by unit of $dz$ , the minimum distance to keep the sampling the same. . . . .	49
2.3 Structure of the operator free space propagation with the angular spectrum of plane waves method. The initial disturbance $U(x, y; 0)$ is transformed into the angular spectrum $A(f_x, f_y; 0)$ with a Fourier transform implemented by a FFT algorithm. The angular spectrum is multiplied by the propagation transfer function $H(f_x, f_y)$ and the resultant angular spectrum is inverse transformed into the output disturbance $U(x, y; z)$ . .	55
2.4 example . . . . .	57
2.5 example . . . . .	61
2.6 Structure of the operator free space propagation with the angular spectrum of plane waves method in its band limited version. The initial disturbance $U(x, y; 0)$ is transformed into the angular spectrum $A(f_x, f_y; 0)$ with a Fourier transform implemented by a FFT algorithm. The angular spectrum is multiplied by the propagation transfer function $H(f_x, f_y)$ whose bandwidth has been limited according to equation 2.63. The bandwidth of the transfer function depends on the sampling of the input field, the wavelength of the light $\lambda$ and the propagation distance. The resultant angular spectrum is inverse transformed into the output disturbance $U(x, y; z)$ . $N$ is the sampling of the input field, $z$ the propagation distance and $\lambda$ the wavelength. . . . .	62

2.7	The maximum spatial frequency is linked to the dimension of the sampling window of the output field $w$ and the propagation distance $z$ . . . . .	64
2.8	example . . . . .	67
2.9	Comparison between the Signal to Noise ratio (SNR) as a function of the propagation distance for the three propagation method seen in section 2.4.1. The BL and the corrected BL methods improve the SNR, that instead drops with the increasing of the propagation distance when the normal AS method is used. . . . .	68
2.10	Thickness of a lens as a function of position along x coordinate. It can be defined in the same way along the y coordinate . . . . .	69
2.11	example . . . . .	71
2.12	A thin lens converts a plane wave into a spherical wave. . . . .	73
2.13	Phase profile of a computer generated lens. The blue line shows the quadratic phase term and the red line shows the same phase term wrapped every $2\pi$ . This wrapping is the source of the aliasing. . . . .	74
2.14	Schematic of the 2f system simulated. f is the focal lenght, z the propagation distances, D is the aperture of the lens, w the field of view and N the sampling resolution. . . . .	77
2.15	Operator sequence for the 2f system. . . . .	78
2.16	From top to Bottom: Image and intensity cross section of a point source according to multi step method, angular spectrum method, band limited angular spectrum method and corrected band limited angular spectrum method. . . . .	80
2.17	From top left to bottom right: Power spectrum of the image of a point source obtained with the multi step Fresnel method, the Angular spectrum method, the band limited angular spectrum method and the corrected band limited angular spectrum method . . . . .	82
2.18	Young experiment setup. . . . .	86
2.19	A random phase mask is generated propagating light coming form an array of sources, each one with a random phase value in the interval $[-\pi, \pi]$ . . . . .	88
2.20	Process of the creation of the phase mask. Top: array of point sources with a random phase value; centre: array of the areas of coherence at source after the convolution with $K$ ; bottom: randomized areas of coherence at object plane after the propagation of $d_o$ . . . . .	90

2.21	Final random phase mask generated by 10, 50, 100 and 200 sources.	91
2.22	Emission spectrum of the LED considered in our simulations and real image system.	93
2.23	example	94
2.24	Signal to noise ratio of the image of a USAF resolution target plotted as a function of the coherence index $C$ .	95
2.25	Images of the USAF resolution target with different values of $\iota$ . Increasing the number of point sources generating the phase mask creates improves the resolution and the contrast	96
2.26	Noise due to the speckles in an image of a USAF resolution target after only 5 iterations.	97
2.27	Images of the USAF resolution target obtained adding an increasing number of snapshot. this is equivalent to increase the integration time of the sensor. The noise due to the speckles caused by the phase mask decreases with increasing number of iterations.	98
2.28	Signal to noise ratio as a function of the number of iterations. The threshold has been calculated looking at the variance of the previous five data.	99
2.29	Comparison between the coherent and an incoherent response of a simple 2f system to a sharp edge.	101

# **Chapter 1**

## **Theory and methods of plenoptic imaging**

### **1.1 Introduction**

A camera is a device that captures light in a scene [33]. The main constituents of a conventional camera are the detector and lens. The rays of light passing through the aperture of the lens are recorded on the sensor as a two dimensional irradiance map of the scene imaged. Therefore a traditional camera performs a limited sampling of the complete set of rays, and in general of the amount of information, contained in the scene [1]. It is interesting to define the total amount of information contained in the light captured by a camera and if there is an effective way to record and extract it. The space is filled with a dense array of light with various intensities [7]. From each point of the object imaged a cone of rays departs and fills the whole space while propagating. If a traditional camera is placed at a certain position from the object it will sample only the rays passing through its aperture. The set of information contained in this cone of rays will than be recorded on a two dimensional plane. This process of recording light coming

## 2 CHAPTER 1. THEORY AND METHODS OF PLENOPTIC IMAGING

from a three dimensional scene on a two dimensional plane causes loss of information. Following Adelson *et al.* [7] all the information carried by the light propagating into space can be described by a function, called plenoptic function. Different parametrizations of the plenoptic are possible. One of these is a four dimensional function called Light Field that will be described in more detail in the next sections. It will also be described a new class of optical instruments, are called computational cameras, that are able to record and extract information from the light field. Computational cameras differ from a conventional camera in the way they sample the light coming from the object using a non conventional new optics that codifies the light that hits the detector. This coded information is then decoded by a computational stage, in order to extract an image [1]. Schematics of the difference between a conventional and a computational camera can be found in figure 1.1

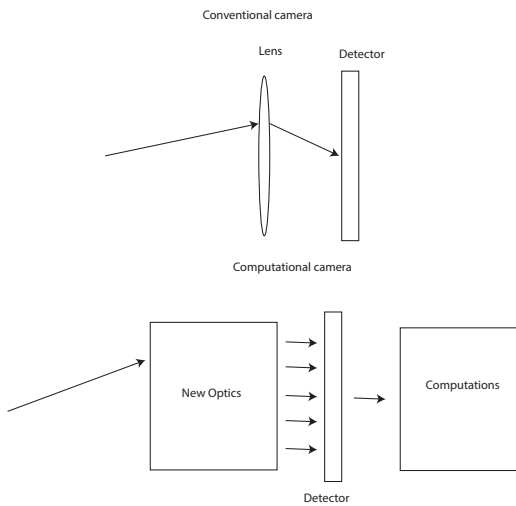


Figure 1.1: Differences between a traditional camera and a computational camera [1].

## 1.2 Plenoptic function and the light field

A black and white photograph taken by a conventional camera represents the intensity of light seen by a single viewpoint, at a single time, averaged and weighted over the wavelengths of the visible spectrum [7]. For each point of the sensor, the intensity can be represented as function of the position  $P(x, y)$ . A colour photograph adds information about the wavelength  $\lambda$  of the light adding a third variable,  $P(x, y, \lambda)$ . If several photos are taken in succession forming a movie the time dependence is added,  $P(x, y, \lambda, t)$  and if the movie is captured using holographic techniques, i.e. saving phase and amplitude at of the optical field, all the information regarding the light intensity observable from any viewpoint  $\vec{V} = (V_x, V_y, V_z)$  is recorded. Therefore to describe all the information that is potentially available from the light coming from the object a seven dimensional function is needed. It takes the name of plenoptic function and its name comes from Latin *plenum* that means full [8, 7, 6]. The plenoptic function implicitly contains a description of every possible photograph that can be taken of a particular scene from any possible point of view. To record the plenoptic function, one should move the camera along all the possible positions  $\vec{X}$  around the object and take a snapshot or have an array of cameras surrounding the object taking snapshots simultaneously. The plenoptic function is an idealized concept and it is impossible to record it completely. However it is possible to acquire samples of it or projection along one dimension. For example a conventional black and white picture is a two dimensional slice along the coordinates  $x$  and  $y$  of the seven dimensional plenoptic function taken from a single point of view, av-

#### 4 CHAPTER 1. THEORY AND METHODS OF PLENOPTIC IMAGING

eraging the wavelength and integrating over the exposure time. A plenoptic camera is able to record a section of the plenoptic function [7]. In particular, it records the part of the plenoptic function whose rays pass through the aperture of the camera, hence all the possible viewpoints contained in the lens aperture. Final images are constructed by sectioning the plenoptic function along certain coordinates. The process of extracting information from the plenoptic function is called rendering [13, 3] and it is where the computational stage operates. Before proceeding in describing a plenoptic camera in detail it is useful to define another parametrization of the plenoptic function derived by Levoy *et al.* that is more useful to implement the computational algorithms in the following sections. This parametrization is called light field and is defined as the radiance as a function of position and direction [13]. It is described by a set of four coordinates, two spatial coordinates and two directional coordinates and for this reason is often referred to as the 4D Light Field. There are two possible representation of the light field: the two point representation and the point-angle representation. With reference to figure 1.2 in the two point parametrization a ray of light is propagating in the free space form the point  $(x,y)$  to the point  $(u,v)$ . Its direction of propagation in three dimensional space is defined by the couple of points where it crosses two parallel planes. Therefore the set of coordinates  $(x,y)$  and  $(u,v)$  defines only one ray of light [13]. The point angle parametrization instead uses the coordinates of the point where the ray intercept a plane perpendicular to the optical axis, and the angles that it forms with the optical axis along the directions  $x$  and  $y$ , namely  $\theta_x$  and  $\theta_y$ , as shown in figure 1.3 [28]. In both cases the intensity is a function of four coordinates.

The 4D light field is therefore:

$$L(x, y, u, v) = L(x, y, \theta_x, \theta_y) \quad (1.1)$$

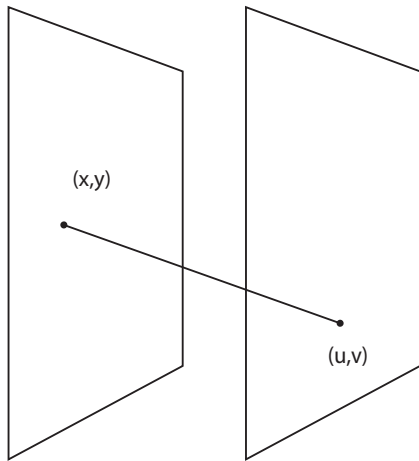


Figure 1.2: Two point representation of light field. Each ray of light is unequivocally defined by the coordinates of two points of interception.

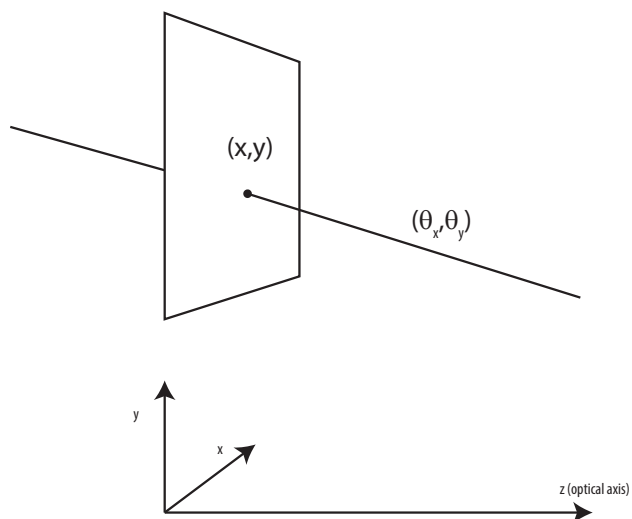


Figure 1.3: Point angle representation. A ray of light is unequivocally defined by the coordinates of a point that belongs to a plane perpendicular at the optical axis  $z$  and by the angles  $\theta_x$  and  $\theta_y$  that it forms with the optical axis along the directions  $x$  and  $y$ .

## 6 CHAPTER 1. THEORY AND METHODS OF PLENOPTIC IMAGING

For each pixel of the sensor of a plenoptic camera it is possible to determine these four coordinates. The information provided by the two extra directional coordinates enables a set of computational features such as 3D reconstruction, synthetic refocus, full depth of field and aberration correction [2]. Each of these features is possible after having decoded the light field with the computational stage as shown in figure 1.1.

### 1.3 Plenoptic camera

A plenoptic camera is a camera that records the 4D light field as described in equation 1.1. The version proposed and built by Adelson and Wang in 1992 [8] is composed of a main lens, a sensor and a micro lens array placed in front of the sensor [8]. The presence of the micro array enables the codification of the directional information on the sensor. This coded image represents the raw data of the plenoptic camera. This kind of camera can be seen in figure 1.4:

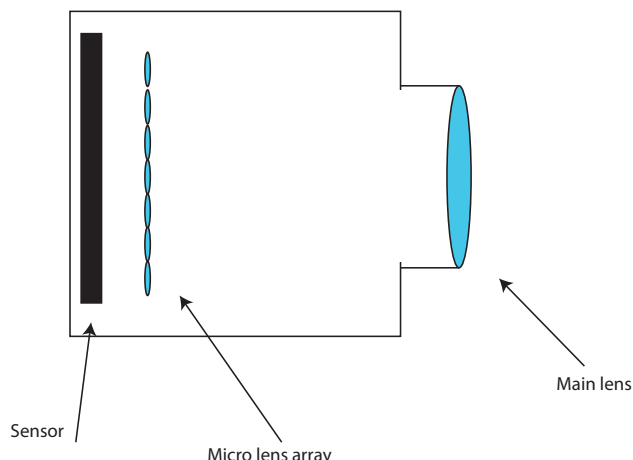


Figure 1.4: Plenoptic camera and its fundamental components. The presence of the micro array allows to record the light field .

The optical performance of the camera depends on the array's design characteristic. The main issue with the micro lens array is its position with respect to the main lens and the sensor. Depending on where it is placed two types of cameras are possible:

- if the main lens forms its image on the micro array and the sensor plane is conjugated with the main lens it is the first generation plenoptic camera, or plenoptic 1.0 [21]
- if the main lens forms its image on a plane that is different from the micro array plane and the micro lenses image the main lens image plane on the sensor it is the focused plenoptic camera, or plenoptic 2.0 [3]

The two different kinds of cameras can be seen in figure 1.5. In the next sections both configurations will be extensively analysed and the way in which they capture the light field will be explained with particular attention to the differences in the raw data they produce. Their performances in term of lateral and directional (or angular) resolution will be detailed. The computational algorithms to render images from the raw data will also be extensively explained.

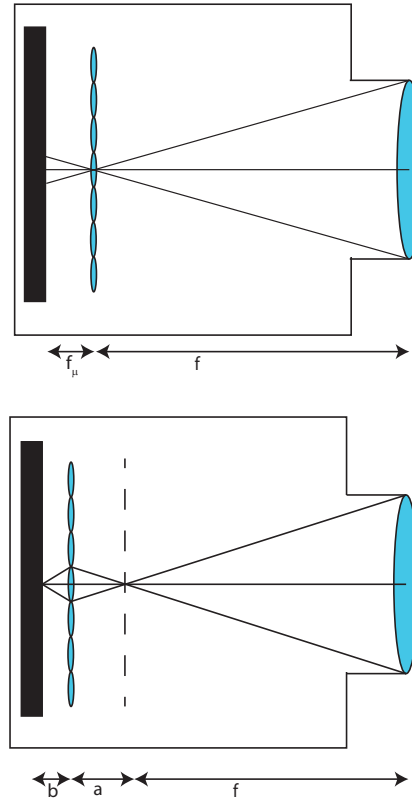


Figure 1.5: Top: Plenoptic camera 1.0. The main lens is focused on the object and forms and image on the micro array and the micro array.  $f$  is the focal length of the main lens and  $f_\mu$  the focal length of the micro lens array. Bottom: Plenoptic camera 2.0. The main lens is focused on an object and forms an image on the plane represented by the dashed line. The micro array acts as a relay between the main lens image and the sensor, since it satisfy the lens equation  $1/a + 1/b = 1/f_\mu$ .

## 1.4 Plenoptic Camera 1.0

The first version of the plenoptic camera has been proposed and realised by Adelson and Wang in 1992 [8] and then improved by Ng *et al.* in 2006 [21, 2]. The purpose of Ng was to design a camera that can use ray tracing techniques to compute synthetic photographs after the acquisition of the four dimensional light field. The main difference between Ng camera and Adelson

and Wang camera is that the latter was a prototype that utilized a system of relay lenses from the main lens image plane and the micro lens array [21] while in Ng camera the array of micro lenses is placed directly in front of the sensor. Each micro lens forms an elemental sub image on the sensor and the directional information is inside the sub images. The main lens focuses the rays coming from one point on the object plane on a single point in the image plane. If an array of micro lenses is placed at this image plane all the rays will end up on a single micro lens. The micro lens will then split this bundle of rays on the sub image underneath it, separating the rays according to their direction. This is explained in figure 1.6 where the plenoptic camera is modelled a simple 2 f system. Since the sensor plane is conjugate with the main lens image under each micro lens there will be an image of the main lens aperture. For simplicity in figure 1.6 the system is composed by only five micro lenses and each sub image is composed of only three pixels. The rays departing from a single point in the object plane shown in blue, red and green, are transferred by the main lens on a single micro lens. As an effect of the micro lens, each ray ends on a different pixel of the micro image.

10 CHAPTER 1. THEORY AND METHODS OF PLENOPTIC IMAGING

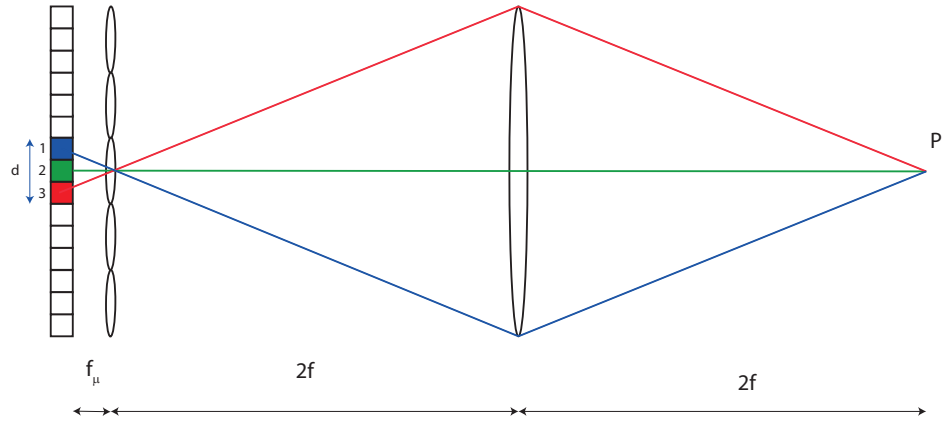


Figure 1.6: Ray diagram of a plenoptic 1.0 system. The main lens is in a  $2f$  configuration and the sensor plane is conjugated with the main lens plane. The micro lens position maps the position  $(x,y)$  of the point  $P$ , while the sub image maps the directions of the rays coming from that point. The ray with direction  $\theta_1$  falls on the pixel 1 (blue), the ray with direction  $\theta_2$  falls on the pixel 2 (green) and the ray with direction  $\theta_3$  falls on the pixel 3 (red). The sub image  $d$  maps the direction of the ray.

Since in figure 1.6 there are only three pixels per micro lens, the maximum number of directions that can be sampled is three. A plenoptic camera samples as many directions as the number of pixels under each lens let, therefore the directional resolution is given by the sub image resolution. Regarding spatial resolution, looking again at figure 1.6 can be noticed that the spatial position of the point  $P$  is recorded at the micro array plane and the sampling of the position is linked to the number of lenses in the micro array. This leads to a trade-off between directional and spatial resolution since due to the finite dimension of the sensor, when more pixels are used to record the direction the same amount of pixel is lost to record the position. A further and more detailed explanation of this will be given in the next paragraph. Now look how the light field is recorded. With reference to figure 1.7 two points are shown at two different positions but on the same focal plane. The

task now is to find a link between Levoy's definition of Light Field, the two point representation [13, 4], and the output data of the plenoptic 1.0 camera. Each sub image under each lens-let is an image of the main lens aperture, while the main lens image is formed on the micro array plane. To define the direction of a ray two points are needed. One point is its origin, the second is where it crosses the main lens. These two points are sampled by the lens let array and by the sub images on the sensor, as shown in figure 1.7. Therefore it is possible to refer to the micro lens position on the array with spatial coordinates  $(x,y)$ , and to the pixels of the sub images as the directional co-ordinates  $(u,v)$ . With an array of  $5 \times 5$  micro lenses and a sensor of  $15 \times 15$  pixel, the 4D light field recorded will be a  $5 \times 5 \times 3 \times 3$  function. Each point of this function is an intensity value identified by four coordinates, 2 spatial and 2 directional. the sampling of the spatial coordinates is  $5 \times 5$ , the sampling of the directional coordinates is  $3 \times 3$ .

## 12CHAPTER 1. THEORY AND METHODS OF PLENOPTIC IMAGING

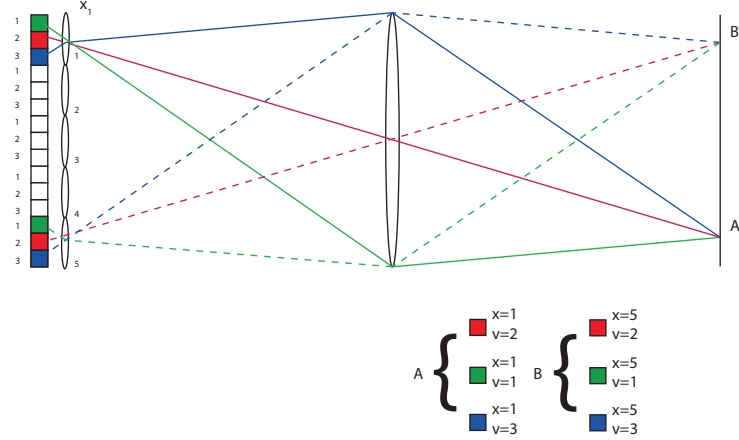


Figure 1.7: Sampling of Light Filed. Each ray is described by a set of four coordinates, two spatial ( $x,y$ ) and two directional ( $u,v$ ). The spatial coordinates are sampled by the position of the lens let in the micro array, the directional coordinates are sampled by the pixel under the lens let. Point A, its position is sampled by the lens let number 1( $x=1$ ), and three rays are green (1,1), red(1,2), blue(1,3). Each ray is defined by  $x$  and  $v$ . Point B:for one position ( $x=5$ ) three rays are sampled green (5,1), red(5,2), blue(5,3), dashed line.

This sampling used in the example above is of course very low. The amount of light captured by a lens is defined by its f-number that is the ratio between the focal length and the aperture. The f-number is proportional to the number of rays with different directions that enter into the main lens aperture. We can also define the relative f-number as the ratio between the distance between the lens and its image, and the aperture.

$$f_{\#} = \frac{z}{d} \quad (1.2)$$

where  $z$  is the distance from the main lens and the image plane and  $d$  its aperture diameter. Another useful quantity to describe the amount of directions sampled by a lens is its numerical aperture, defined, referring to figure

1.8 as:

$$NA = n \sin(\theta) \simeq n\theta = \frac{2}{f_{\#}} \quad (1.3)$$

Where  $n$  is the index of refraction, and  $\theta$  is half the total range of direction sampled by the lens. In air  $n=1$ , therefore the relation between the f-number and the range of directions is given by:

$$\Delta\theta = 2\theta = \frac{4}{f_{\#}} \quad (1.4)$$

To be sure that all the directions sampled by the main lens are mapped into the light field, the f-number of the lens let should match the f-number of the main lens [21] as shown in figure 1.8. This condition known as f-number matching is very important in plenoptic imaging. If the f-number of the lens let is smaller than the one of the main lens then there is an under sampling of the rays intercepted by the main aperture, since some of the pixels remain dark. If the f-number of the lens let is bigger on the other hand there is cross-talk between the sub images. In both cases directional information is in part lost (figure 1.9) .

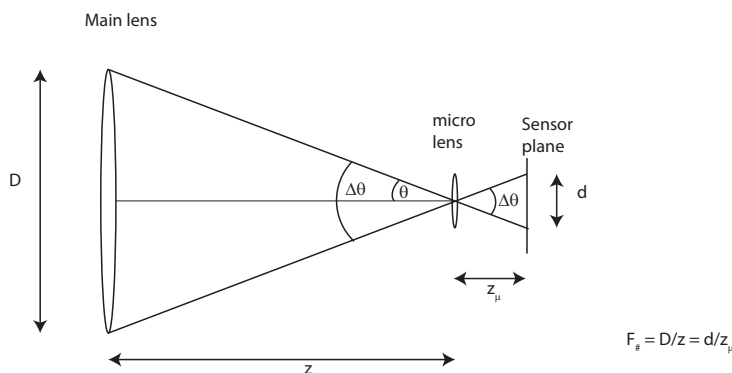


Figure 1.8: F-number matching between the main lens and the micro lens in the array.

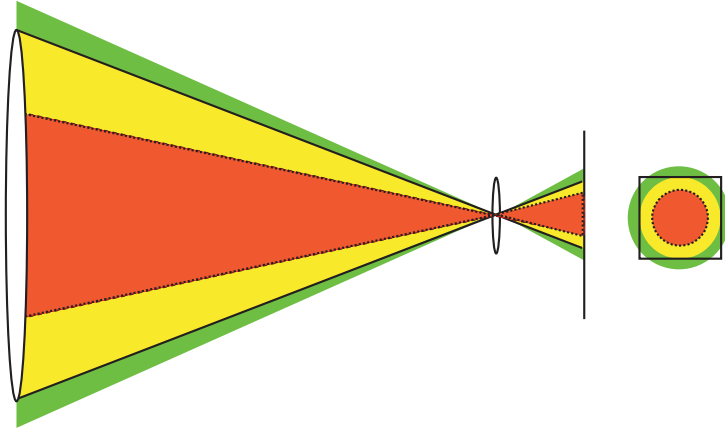


Figure 1.9: When the f-number is matched, all the rays captured by the main lens are mapped on the sub image (yellow). If the f-number is smaller (red), the sub image is smaller and there is an under sampling of the set of rays. If the f-number of the lens let is bigger (green), the sub image is larger and cross talk happens between near sub images .

### 1.4.1 Phase space in plenoptic 1.0

It is very useful to analyse the sampling of the light field under a phase space point of view. In figure 1.10 a point source is sampled by the lens let array. Here it is considered the mono dimensional case for simplicity. The single ray departing form the point  $P$  on the focal plane of the main lens is refracted by the optical system and is captured by a pixel on the sensor that belong to the sub image of a lens let. The sub image position on the array gives the coordinate  $x$ . The pixel of the sub image gives the direction  $\theta_x$ . Therefore in the phase space a single ray is represented by a point with coordinates  $(x, \theta_x)$ . Considering all the rays departing from the point  $P(x)$  captured by the main lens, they will all be focused on a single lens let and then split on the sub image. Each pixel of the sub image corresponds to a different direction (ray). In the phase space this is equivalent to a vertical line. The

physical meaning is that to single spatial position  $x$  corresponds a range of  $\Delta\theta_x$  possible different directions, defined by the numerical aperture of the main lens matched with the one of the lens let.

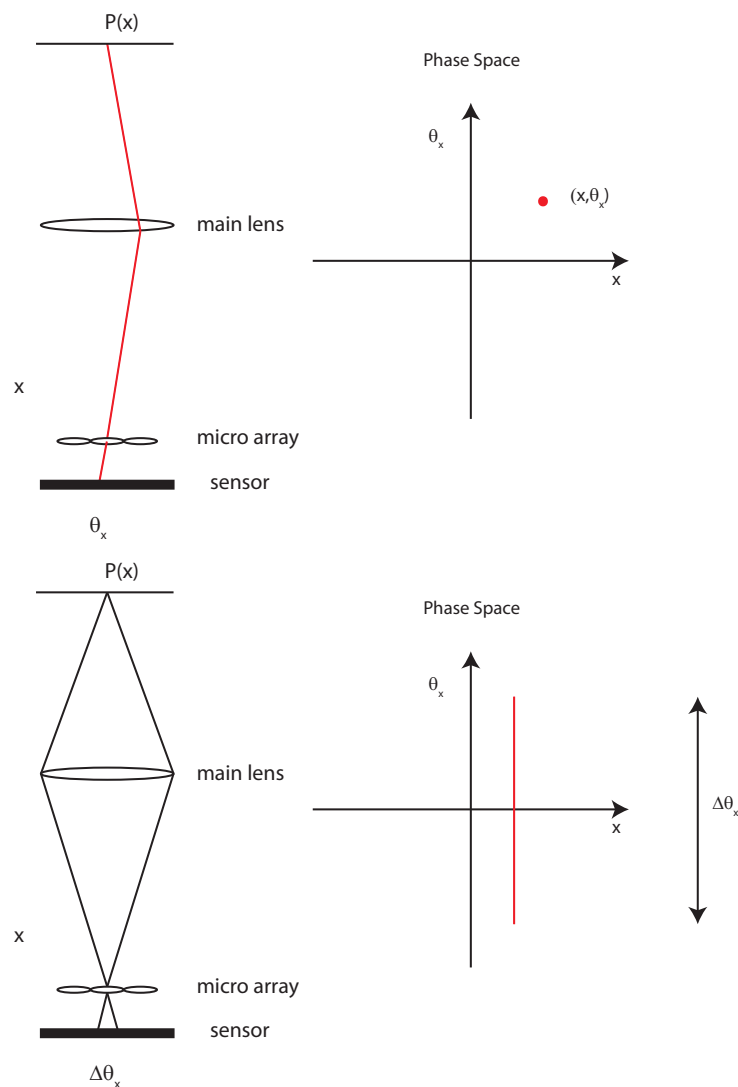


Figure 1.10: Sampling of the light field and phase space representations of the rays.

### 1.4.2 Light Field Parametrization

Before discussing the rendering procedures for plenoptic 1.0 light field data there will be described the three different parametrizations of the light field from the raw image. A plenoptic 1.0 raw image looks like an array of sub images, each sub image contains samples of direction. An example of a plenoptic raw image can be seen in figure 1.11, while in figure 1.12 it is shown in detail how a sub image appears. The raw image has been generated simulating light propagating into a plenoptic camera, using a Matlab toolbox developed as part of this work which is described in detail in chapter 2. The camera is composed of a 60 mm lens, with an aperture of 7 mm, and a sensor with a resolution of 1500 by 1500 pixel. The micro array is composed of 75 by 75 lens let with a focal length of 5 mm. The object imaged is a flat two dimensional image, therefore no depth information is stored.

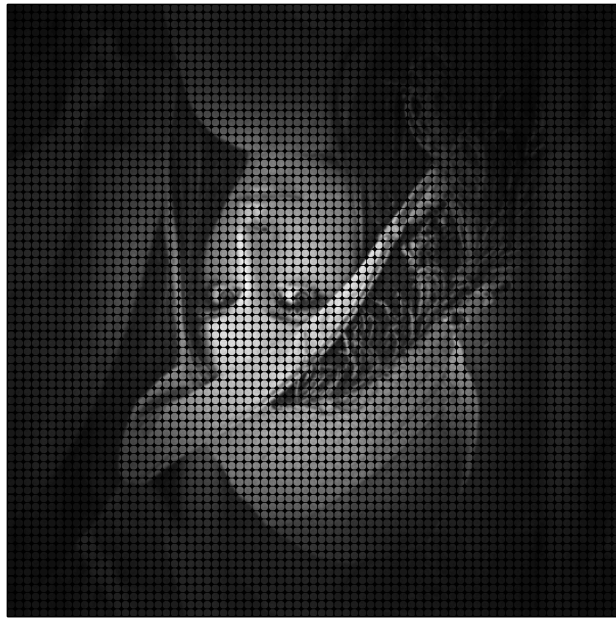


Figure 1.11: Example of a raw plenoptic 1.0 image.

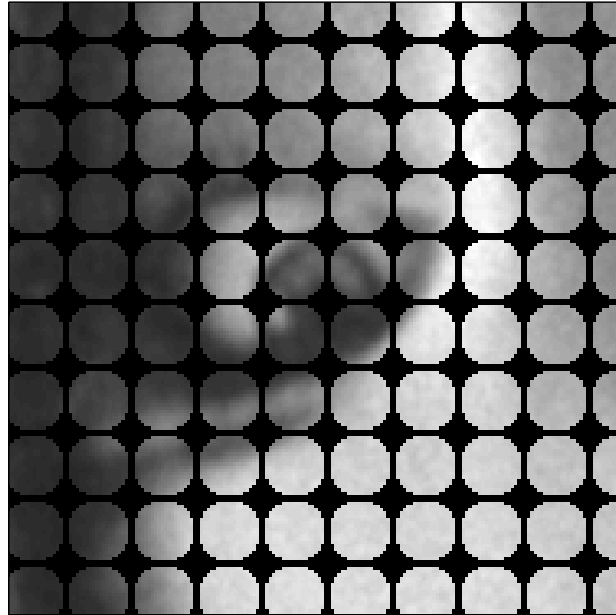


Figure 1.12: Zoom on the raw image. Each lens-let is formed by  $20 \times 20$  pixels. Each pixel represents a direction of the rays hitting the lens let that produced the sub image.

This raw image is the first parametrization of the light field and it is called camera view. Pixels are arranged according to the positional coordinates, and each sub image contains the directional coordinates as shown in figures 1.11 and 1.13. A second parametrization, known as array view, is obtained by rearranging the pixels according the directional coordinates [2]. The result is an array of  $N \times N$  sub images, where  $N$  is the number of samples of the directional coordinates. Each sub image represents the point of view linked with a direction  $(\theta_x, \theta_y)$ . The array view can be seen in figure 1.14 and 1.15 while the method to pass from the camera view to the array view is illustrated in figure 1.13.

18 CHAPTER 1. THEORY AND METHODS OF PLENOPTIC IMAGING

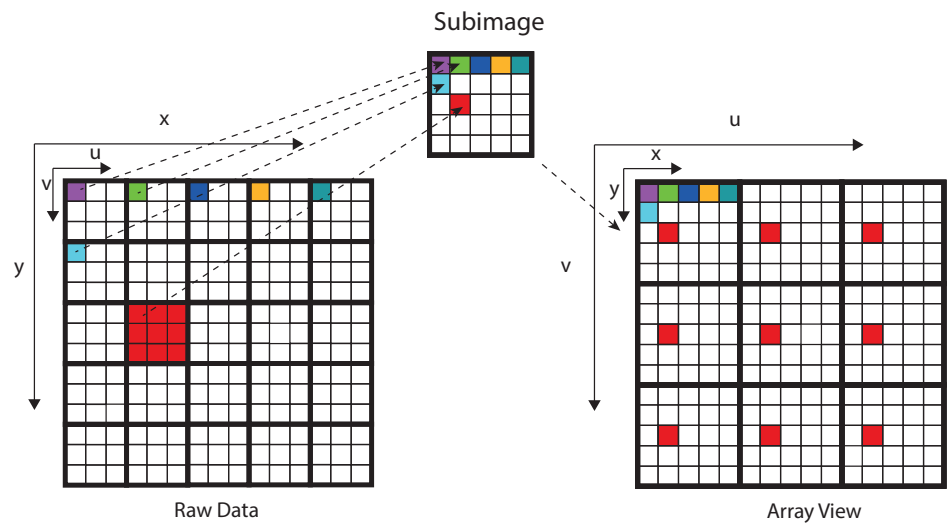


Figure 1.13: The array view is an array of the different point of view obtained rearranging the pixels according to the directional coordinates.

An example of the array view parametrization of the raw image in figure 1.11 is shown in figure 1.14.

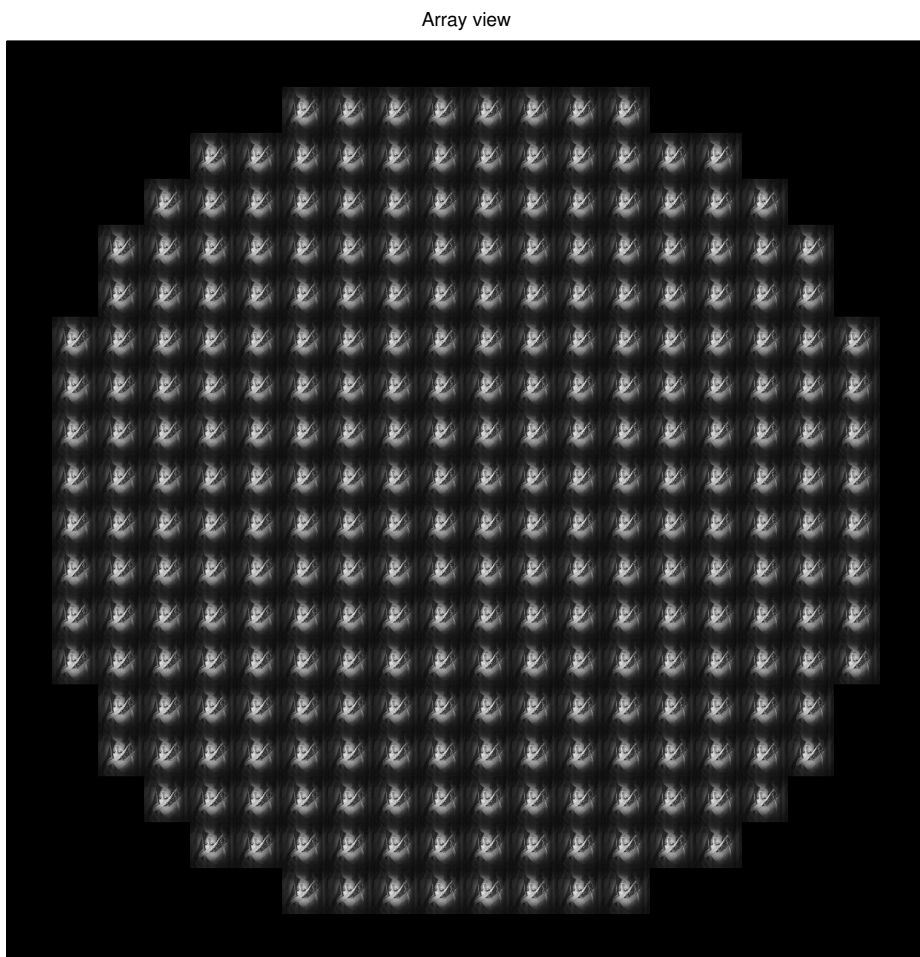


Figure 1.14: The array view is an array of the different points of view obtained by rearranging the pixels according to the directional coordinates.



Figure 1.15: Zoom of the central part of the array view showing in detail the different points of views.

The third and last parametrization of the light field, is the 4 D radiance, a four dimensional function that represents radiance as a function of position and direction. [13]. This third parametrization is less intuitive but is very useful from a computational point of view since it is a four dimensional array, and every ray can be addressed by a set of four coordinates, or indices, as will be explained in detail in chapter ??.

## 1.5 Plenoptic 1.0 rendering

The act of de-codifying the information present on the sensor of the plenoptic camera in order to get an image is called rendering. In a conventional 2D image the intensity of each single pixel, corresponding to a position, is obtained summing the contributions of all the rays of light converging to that point of the sensor [3] as shown in figure 1.16. This is equivalent to integrate for each position all the possible directions of the light field.

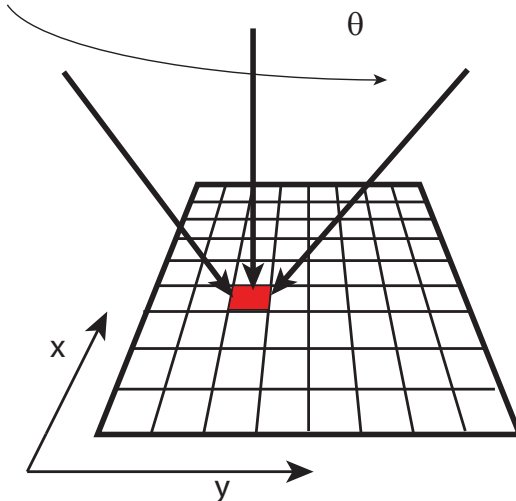


Figure 1.16: Sampling of the light field and phase space representations of the rays.[2]

The same is valid for a computational image, where the integration are made in post processing from the raw plenoptic data captured. If  $L(x, y, u, v)$  is the sampled 4D light field, the radiance  $E(x, y)$  on a pixel  $(x, y)$  of the final rendered image will be given by integrating all the rays coming from all the sampled directions  $(u, v)$  for any fixed point  $(x, y)$ . Following the work of Ng

*etal.* [2] we have:

$$I(x, y) = \frac{1}{z^2} \iint L(x, y, u, v) A(u, v) \cos^4 \theta dudv \quad (1.5)$$

Where  $z$  is the distance between the main lens and the sensor,  $\Theta$  is the angle formed by the rays and the sensor normal and  $\cos^4 \Theta$  is the vignetting factor that takes into account the reduced effects of the rays striking the sensor from oblique directions.  $A(u, v)$  is an aperture function that limits the directions upon which integration takes place to the ones included in the aperture of the main lens. In the paraxial approximation, the  $\cos^4 \Theta$  term can be dropped as well as the  $1/z^2$  term and equation 1.5 becomes:

$$I(x, y) = \iint L(x, y, u, v) A(u, v) dudv \quad (1.6)$$

From a computational point of view, since the samples are discrete, the double integral becomes as a sum along the directional coordinates  $u$  and  $v$ . The total intensity of each pixel of the rendered image is then the sum of the intensities of the pixels that form the correspondent sub image divided by the number of pixels in the sub image. For a light field with  $N \times N$  directional samples, the intensity  $I(x, y)$  is given by:

$$I(x, y) = \frac{1}{N^2} \sum_{i=0}^N \sum_{j=0}^N L(x, y, i, j) \quad (1.7)$$

This can be seen very clearly in the phase space where each pixel of the final image is made by the mean of all  $N$  directional samples [3], as shown in figure 1.17.

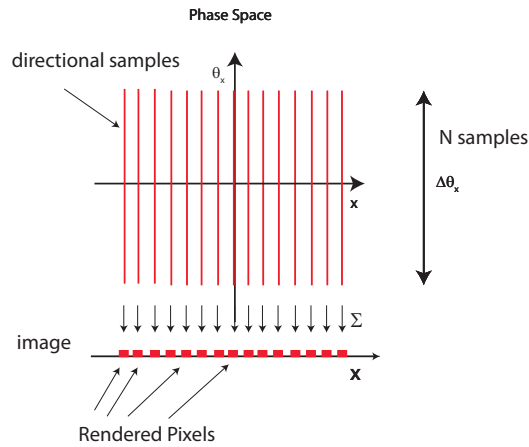


Figure 1.17: Rendering an image from plenoptic 1.0 raw data is equal to summing all the directional samples for each position. This process is shown for the the  $(x, \theta_x)$  slice of the phase space. [3]

Looking at figure 1.17 can be noted that rendering an image from a light field captured by a plenoptic 1.0 camera causes a loss of resolution if compared with the image collected by a conventional camera using the full sensor. Each pixel of the final image correspond to one lens let. Considering a plenoptic camera composed by a sensor with a resolution of  $1000 \times 1000$  pixels and a micro lens array of  $100 \times 100$  lens lets, each sub image will contain  $10 \times 10$  directional samples. All these samples will contribute in computing the intensity of a single pixel, therefore there will be only one pixel per lens let in the final image whose resolution is  $100 \times 100$  pixels. This is the main limitation to plenoptic 1.0 cameras, the better the directional information are sampled, the more spatial resolution is lost. [3, 2]. An example of a rendered image from a computer generated light field is shown in figure 1.18



Figure 1.18: rendered image form the raw data in figure 1.11. Resolution is only  $75 \times 75$  pixel.

This loss of resolution arises from the fact that the lenslet array is not focused on the sensor and it produces on the sensor a blurred image [3].

## 1.6 Plenoptic Camera 2.0

A new kind of plenoptic camera, named focused plenoptic camera or plenoptic camera 2.0, has been proposed by Georgiev and Lumsdaine *et al.* [34, 35]. As shown in figure 1.5 the plenoptic camera 2.0 is based on an array of micro lenses focused on the image plane of the main lens. In this configuration the sensor plane becomes conjugated with the main lens image plane. As will be discussed in the next sections, in a plenoptic 2.0 camera exists a flexible trade-off between angular and spatial resolution [3] leading a full sensor resolution

in the final image [36, 37]. There are two possible configurations of the plenoptic 2.0 camera, as shown in figure 1.19. In both configurations each micro lens forms on the sensor a relay image of part of the main lens image. The position of the micro array is determined to satisfy the lens equation  $1/a + 1/b = 1/f_\mu$ , where  $a$  is the distance from the main lens image plane to the micro array,  $b$  is the distance from the micro array to the sensor plane and  $f_\mu$  is the focal length of each micro lens. If  $b$  is bigger than the focal length  $f_{mu}$  the camera is in a "Copernican configuration" where the main lens image is a real image in front to the micro array, while if  $b$  is smaller than  $f_{mu}$ , the distance  $a$  happens to be negative and the main lens image is formed behind the sensor plane. This is called "Galilean configuration" and the micro array images on the sensor a virtual main lens image.1.19[3].

## 26CHAPTER 1. THEORY AND METHODS OF PLENOPTIC IMAGING

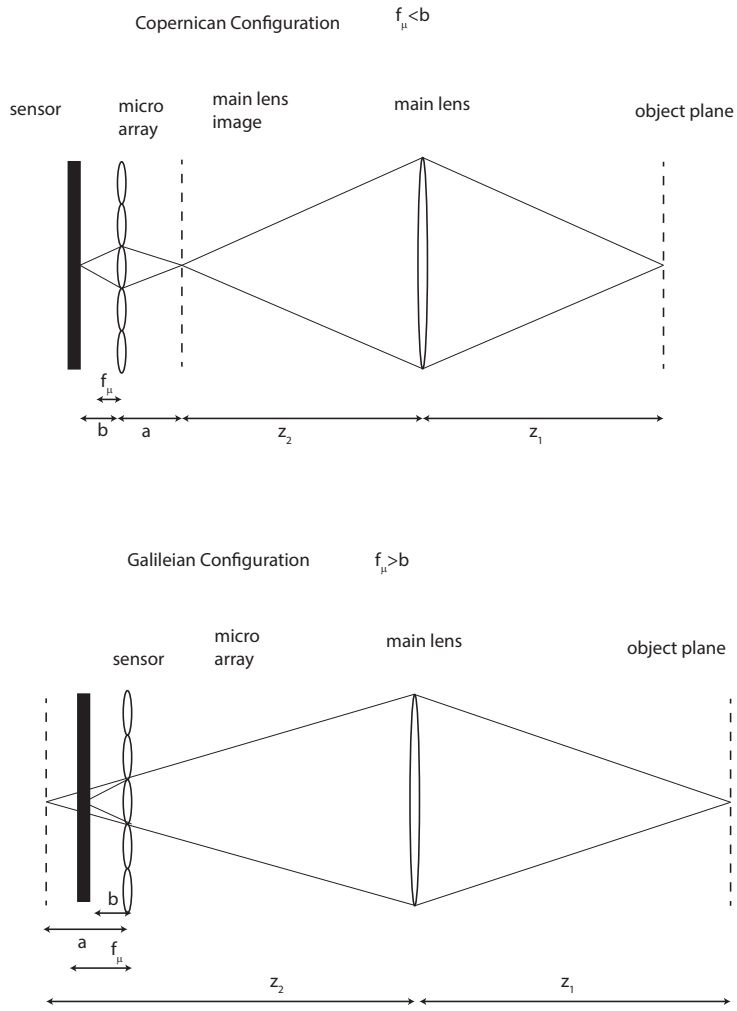


Figure 1.19: If the main lens image is formed in front of the micro array the configuration is called "Copernican", top, and the focal length of the micro array is smaller than the distance  $b$ . If the main lens image is formed behind the micro array the configuration is "Galilean", on the bottom, and the focal length of the micro array is bigger than the distance  $b$ .

For both configurations the magnification of micro array stage is:

$$m = \frac{b}{a} \quad (1.8)$$

The ratio between the distances  $a$  and  $b$  plays a crucial role in sampling the light field in the plenoptic camera 2.0. Figure 1.20 shows a raw plenoptic 2.0

image of a point source acquired simulating a system as it will be explained in chapter 2. The system is composed by a main lens with a focal length of 60 mm, in a 2f configuration and a micro array made of  $150\mu m$  diameter lens lets with focal length of 5.3 mm. The distances  $a$  and  $b$  are set in order to have a magnification  $m$  of 0.3. In this configuration each point of the main lens image is sampled by three lens lets and each sub image corresponds to a point of view of the object. The number of points of view depends on the magnification of the micro array stage. Hence, in order to have more than one point of view recorded it is necessary that the magnification  $m$  is less than one. Looking at figure 1.20 the raw image is composed by a  $3 \times 3$  matrix of sub images, three points of view in the x direction and three along the y direction. Figure 1.21 shows central  $5 \times 5$  sub images in the raw data. The central sub image records the direction corresponding to the central point of view, indicated in both figures with the number 2. The lens lets respectively on the left and on the right of the central one record the directions corresponding to the point of views to from the left, indicated with 1 in figure 1.22, and right, indicated with 3. We can see how the sub images 1 and 3 are shifted towards the outer edge of the sub image. This happens as an effect of the change in the point of view as well as because the sub images are flipped upside down as an effect of the imaging law.

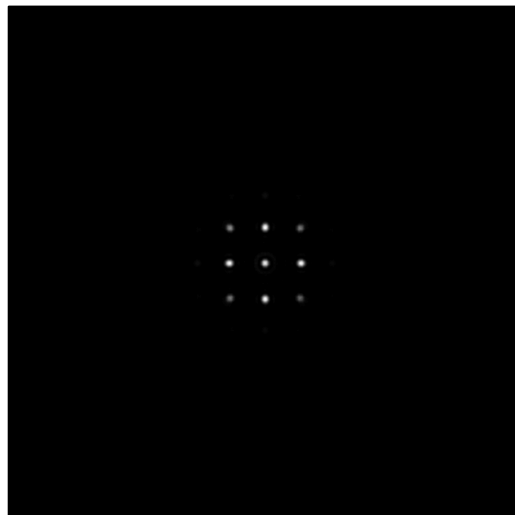


Figure 1.20: Raw data of a point source sampled by a plenoptic 2.0 system with a magnification of the micro array stage equal to 0.3. Data acquired with numerical simulations.

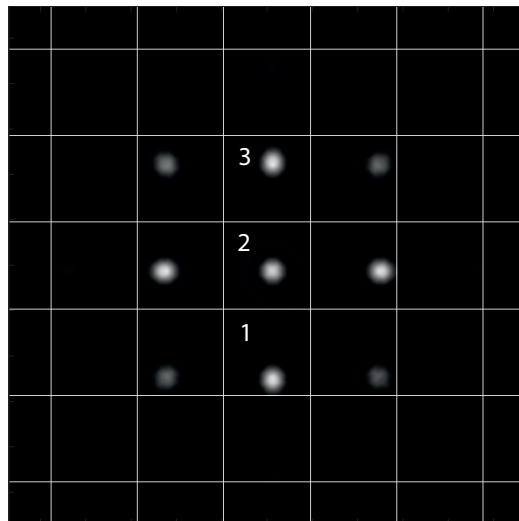


Figure 1.21: Zoomed Raw data of a point source sampled by a plenoptic 2.0 system with a magnification of the micro array stage equal to 0.3. Data acquired with numerical simulations. The grid represent the boundaries of each sub image to show how the point of view of the point source changes across the lens lets. The sub images are shifted by a quantity proportional to the position of the lens let in the array.

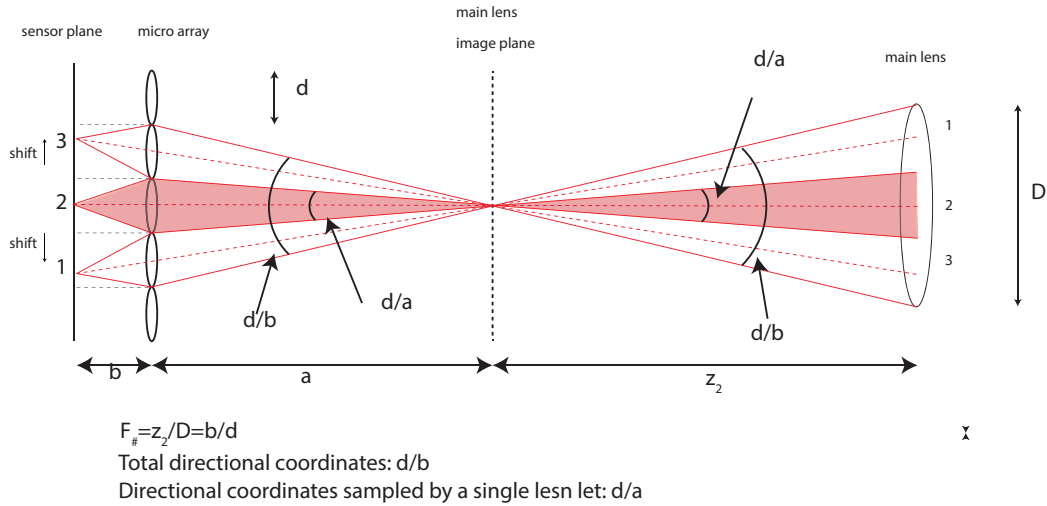


Figure 1.22: Sampling of the light field by a plenoptic 2.0 system. The one dimensional case is shown. Each micro lens has a diameter equal to  $d$ , a focal length  $f_\mu$ , and images the main lens image on the sensor according to the lens law  $1/a + 1/b = 1/f_\mu$ . The total range of directions that can be sampled is given by  $d/b$ . Each lens let samples a sub set of directions equal to  $d/a$  as a single direction. The range of directions shown in red are sampled by the central micro lens as a single point of view. The angular resolution is therefore  $d/a$  and the total number of directional sampled is 3.

As in the 1.0 case, the f-number of the micro lenses matches the f-number of the main lens. Referring to figure 1.22, because of the f- number matching condition, the total number of directions captured by the main lens is defined as  $P = D/z_2 = d/b$  where  $D$  is the aperture of the main lens,  $z_2$  the distance of the main lens image,  $d$  is the diameter of the lens let and  $b$  is the distance between the lens let and the sensor. The amount of directions captured by a single lens let is equal to  $p = d/a$ . Hence the range sampled by the single lens let with respect to the total range of directions in the light field is:

$$\frac{p}{P} = \frac{d}{a} \frac{b}{d} = m \quad (1.9)$$

Hence:

$$p = \frac{b}{a}P = mP \quad (1.10)$$

Therefore the magnification of the lens let array determines the angular resolution of the plenoptic 2.0 system. In the case illustrated in figures 1.23 and 1.22 for each position  $x$  on the main lens image plane, 3 directions are sampled. Regarding the spatial resolution of the rendered image, since the main lens image is scaled by the lens lets by a factor of  $m$ , the resolution of the rendered image will be  $b/a$  times the resolution of the full sensor. This fact implies that the spatio-angular trade off of the plenoptic 2.0 camera is not fixed by the number of micro lenses, but it is determined by the optical geometry of the micro lens stage, and is fully determined by the magnification  $m = b/a$ . The more samples of the directional coordinates, the less will be the spatial resolution of the rendered image. In section 1.7 a more rigorous proof of this will be given. Figure 1.23 shows the effect of magnification on the raw image of a point source. If the magnification is 1, the main lens image is replicated on the sensor under only one lens let. No further information is given by the micro array stage. The whole range of directions is sampled by a single lens let and with only one point of view it is not possible to recover the directional information. In order to have more than one point of view,  $m$  should be at least 0.5. In this case the point source is replicated under a total of four lens lets giving 2 by 2 points of view to render the image. If the magnification decreases further, the number of points of view increases. We can state that the directional information in plenoptic 2.0 is recorded not by a single lens let like in the 1.0 case, but across many lens lets, since each point of the object plane is imaged by a number of lens lets proportional

to the inverse of the magnification 1.8. Each of this lens samples a part of the directional coordinates contained into the light field equal to  $d/a$ . The more point of view are presents, the smaller will be the quantity  $d/a$ , and therefore, the better will be the angular resolution. [35]

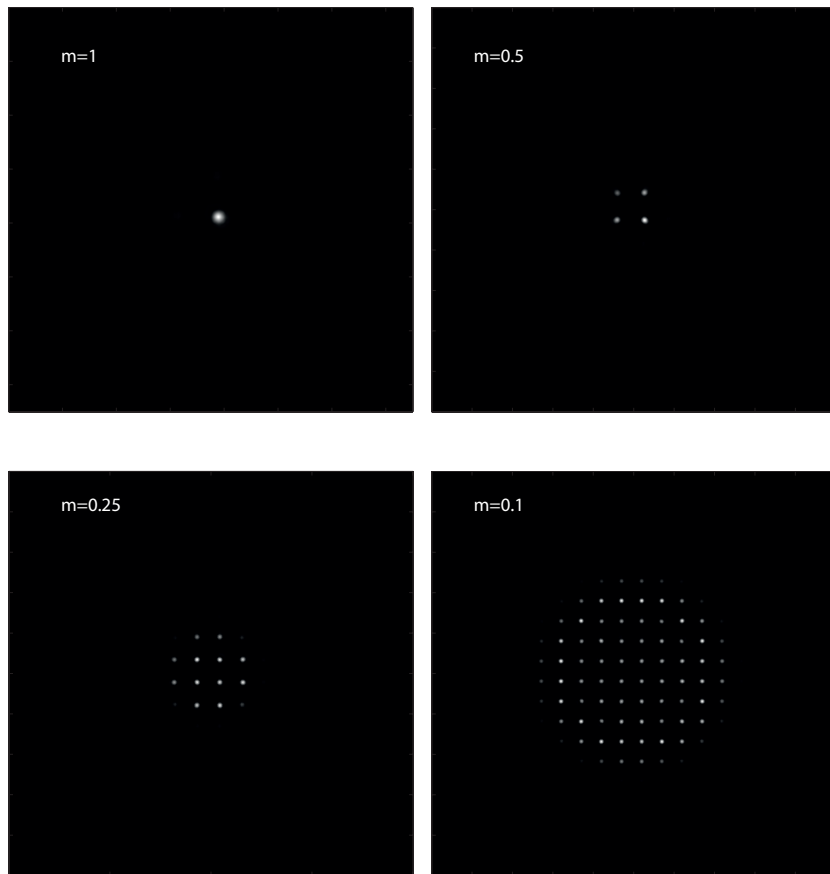


Figure 1.23: Raw images of a point source simulated with different magnifications. From top left to bottom right:  $m = 1$ ,  $m = 0.5$ ,  $m = 0.25$ ,  $m = 0.1$ .

## 1.7 Plenoptic camera 2.0: a geometrical optics analysis

This section provides a mathematical proof of the concepts introduced in section 1.6. The mathematical model of Light Field sampling in plenoptic 2.0 has been developed by Lumsdaine and Georgiev [35, 34]. The goal of this chapter is to express the intensity profile present on the sensor as a function of the light field at the focal plane of the main lens. The intensity on the sensor is given by integrating along all the rays, or the directions, the light field at the sensor in analogy with what discussed in 1.5:

$$I(x, y) = \iint_{\theta_x, \theta_y} L(x, y, \theta_x, \theta_y) d\theta_x d\theta_y \quad (1.11)$$

For simplicity only one positional coordinate  $x$  is considered, and its corresponding direction will be described by a new coordinated called *momentum*, in analogy with Hamiltonian mechanics, defined as:

$$p_x = n\theta_x \quad (1.12)$$

$n$  is the refractive index of the medium of propagation, assumed to be homogeneous. The reason of this change in coordinates is that using the momentum  $p$  the transformations matrix of the optical elements are invertible, and the calculations are simpler [38]. The one dimensional intensity profile is then equal to:

$$I(x) = \int_{p_x} L(x, p_x) dp_x \quad (1.13)$$

In the phase space the rays composing the light field, will be represented by points with coordinates  $(x, p_x)$ . Given a ray  $\overrightarrow{X_0} = (x, p_x)$ , it is possible to

define an arbitrary matrix  $A$  describing the transformation the ray undergoes while propagating in an optical system as:

$$\vec{X}_1 = A\vec{X}_0 \quad (1.14)$$

Where  $\vec{X}_1$  is a vector representing the ray after the transformation  $A$ . The transformation matrix has been defined with the property of having  $\det(A)=1$ , and being invertible it is possible to express the ray  $\vec{X}_0$  as a function of  $\vec{X}_1$  as:

$$\vec{X}_0 = A^{-1}\vec{X}_1 \quad (1.15)$$

The same considerations can be made for the full set of rays composing the light field. In the hypothesis of zero loss during the propagation, the total light field  $L$  is conserved, and  $L(\vec{X}_0)$  equals  $L(\vec{X}_1)$ . Therefore:

$$L_1(\vec{X}_1) = L_0(\vec{X}_0) \quad (1.16)$$

Because of equation 1.14 the Light Field at the position  $\vec{x}_1$  is :

$$L_1(A\vec{X}_0) = L_0(\vec{X}_0) \quad (1.17)$$

For the ray  $\vec{X}_1 = A\vec{X}_0$ :

$$L_1(\vec{X}_1) = L_0(A^{-1}\vec{X}_1) \quad (1.18)$$

For the generic ray  $\vec{X}$  the light field transformation formula becomes:

$$L_1(\vec{X}) = L_0(A^{-1}\vec{X}) \quad (1.19)$$

Equation 1.19 shows the link between the light field at a plane, with the same light field after an arbitrary optical transformation. Referring to figure 1.24

a single lens let of diameter  $d$  is shown and the light field at the sensor plane  $L_b(x, p_x)$  is expressed as a function of the coordinates of the light field at the main lens image plane  $L_a(x, p_x)$ . The link between the two light fields is given by equation 1.19. According to geometrical optics, and as is explained in [39], the optical transfer matrix  $A_{ab}$  from the main lens image plane and the sensor is the composition of two free space propagation matrix and an lens matrix.

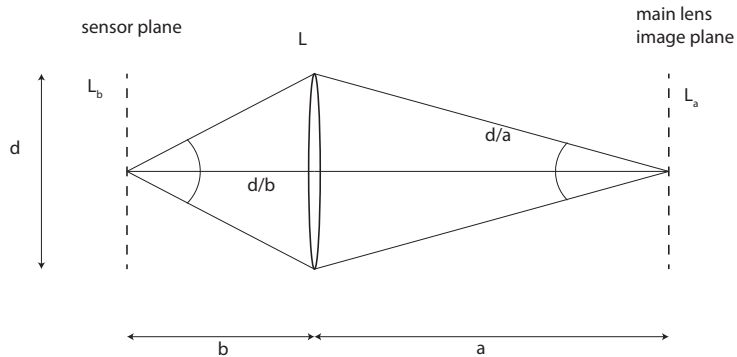


Figure 1.24: System formed by a single lens let. The rays at the main lens image plane are transformed into the rays at the sensor plane by the lens let. The transformation can be described by a matrix  $A$ .

We have:

$$A_{ab} = \begin{bmatrix} 1 & b \\ 0 & 1 \end{bmatrix} \begin{bmatrix} 1 & 0 \\ -\frac{1}{f_\mu} & 1 \end{bmatrix} \begin{bmatrix} 1 & a \\ 0 & 1 \end{bmatrix} = \begin{bmatrix} -\frac{b}{a} & 0 \\ -\frac{1}{f_\mu} & -\frac{a}{b} \end{bmatrix} \quad (1.20)$$

Its inverse is:

$$A_{ab}^{-1} = \begin{bmatrix} -\frac{a}{b} & 0 \\ \frac{1}{f_\mu} & -\frac{b}{a} \end{bmatrix} \quad (1.21)$$

Applying the inverse  $A^{-1}$  matrix in equation to equation 1.19 and substituting into the integral in equation 1.11, the intensity on the sensor behind a single lens let is:

$$I(x) = \int_{p_x} L_a\left(-\frac{a}{b}x, -\frac{b}{a}p_x - \frac{1}{f}x\right) dp_x \quad (1.22)$$

From figure 1.24, for a single spatial coordinate  $x$  on the main lens image plane the integration takes place on a range of directional coordinates  $p_x$  equal to  $d/b$  and the result is:

$$I(x) = \frac{d}{b} L_a\left(-\frac{a}{b}x, -\frac{1}{b}x\right) \quad (1.23)$$

From equation 1.23 the micro lens maps the spatial coordinates on the main lens image plane to the sensor with a scaling factor equal to the magnification  $m = b/a$ . Therefore the resolution of the sampled light field on the sensor is  $b/a$  times the resolution of the sensor. The directional coordinates are mapped as  $x/b$ . If the lens let diameter is  $d$  then the maximum number of directional coordinates sampled by one lens let is equal to the f-number of the lens let  $d/b$ . Figure 1.24 shows how a single micro lens samples the radiance from a single point  $X$  on the main lens image plane. Each pixel of the micro lens image samples a single position  $X$  and a span of  $d/a$  directional coordinates  $p_x$ . The same position  $X$  is sampled also by other micro-lenses as shown in picture 1.25, but since each micro lens only captures  $d/a$  samples of the directional coordinates, each lens let samples a different portion of the total span directional coordinates contained in the light field.

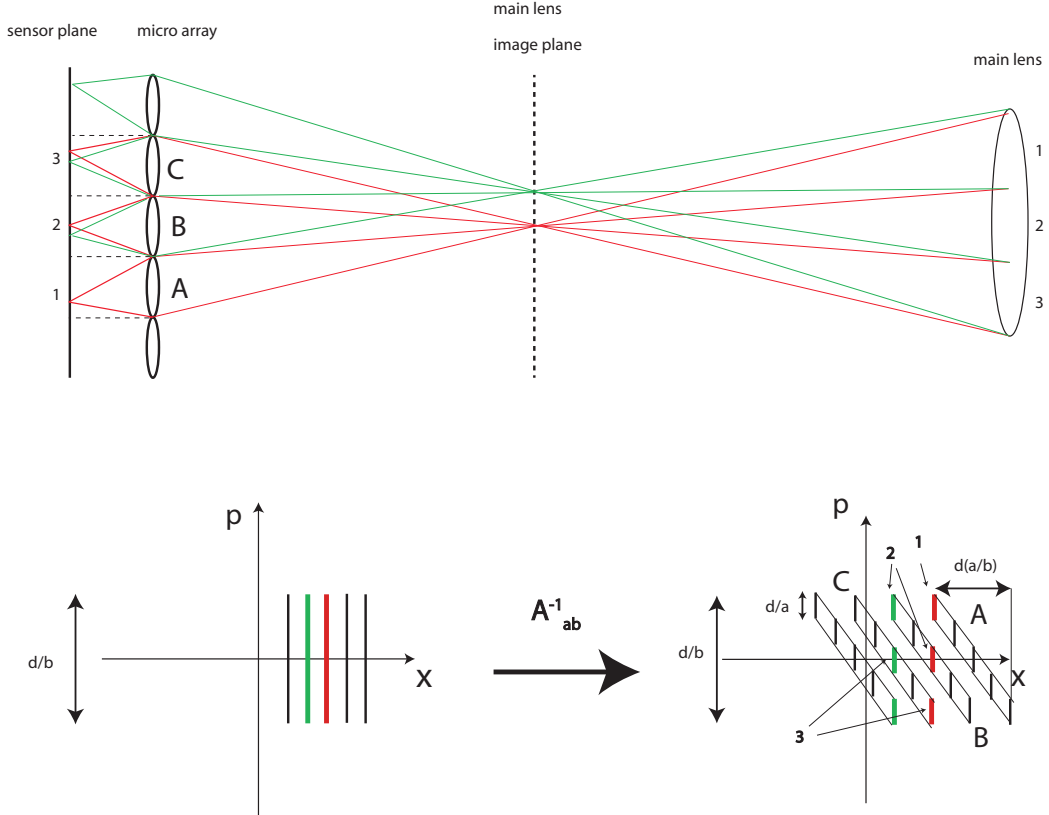


Figure 1.25: Sampling of the light field by plenoptic 2.0 camera. For each of the two points represented, red and green, The total range of directional coordinates are sampled by three different lens lets. For one position three directions are sampled, with a resolution of  $d/a$ . Therefore the directional sampling in plenoptic 2.0 is made across many lens lets. This can be seen in the phase space. Lenset B and C sample 2 directions indicated with the same number in the ray diagram and the phase space. Lens let A only samples one direction of the red point.

## 1.8 Plenoptic 2.0 rendering

The basic rendering in plenoptic 2.0 cameras is still made by integrating all directions associated to a single position, as shown 1.8. The difference with plenoptic 1.0 rendering is that this time the directional coordinates for a single position,  $d/b$ , are recorded across many lens lets, each sampling  $d/a$

coordinates and as a consequence of that, the integration takes place across all of these micro lenses [28]. The basic rendering process is shown in figure 1.26.

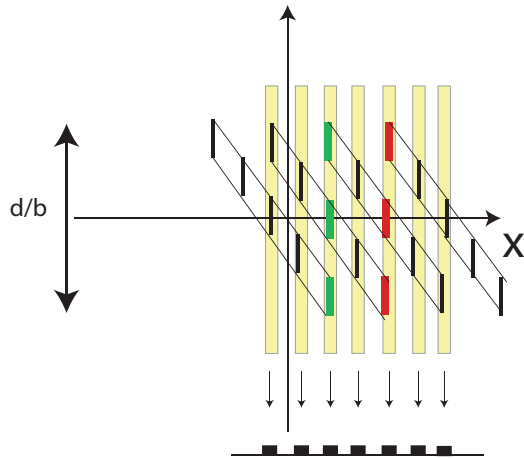


Figure 1.26: Image rendering with the focused plenoptic camera. One pixel of the rendered image is given by the integration on all the directions  $d/b$  associated with a given position. The integration takes place across the lens let.

rendering an image in plenoptic 2.0 is more complicated and less intuitive than the 1.0 case, therefore a more detailed analysis of plenoptic 2.0 rendering will be given in chapter ??.



# Chapter 2

## Fresnel Simulation Toolbox

### 2.1 Introduction

In this chapter will be described a MATLAB simulation toolbox developed as a part of this doctorate project in order to investigate the potentiality of plenoptic imaging for biomedical and microscopy applications with particular interest in its behaviour at the diffraction limit. In literature can be found many works on simulating plenoptic imaging devices. When this project began in 2012 there were few works that analysed the behaviour of a plenoptic camera under a wave optics approach and the majority of the literature treated the plenoptic system under a ray tracing approach. Then in the last years various research groups developed independently Fresnel wave optics analysis of plenoptic 1.0 imaging systems, such as Schroff *et al.* [40, 30] and Trujillo-Servilla *et al.* [41] and a Fourier optics approach of the diffraction limit of a digital camera, Farrell *et al.* [42]. In this work a Fresnel optics approach has been applied to a plenoptic camera with purpose of understanding how the light field is recorded and to define some guidelines to design a working setup. Particular attention has been dedicated to the

behaviour of the system at its diffraction limit, subject that has never been explicitly treated in literature. In this chapter there will be exposed four different methods to simulate light propagation in an optical system and it will be described and compared their performance in term of accuracy of the results, noise and computational effort. A Fresnel optics approach has been chosen because the simulation tool to describe a plenoptic imaging system has to the following requirements:

- It has to preserve the phase of the optical field propagating in order to preserve directional information of the rays of light;
- It has to take into account the effects of diffraction;
- It had to be adaptable in order to easily change the characteristic of the optical system, trying various configurations, keeping the operator based approach of ray tracing.

To address these features, a wave optics simulation toolbox has been designed and developed. Most of the existing literature on simulating plenoptic system are based on ray tracing techniques [43, 44, 45, 2, 13]. The advantages of using ray tracing is that the transformations that rays undergo during the propagation can be described by two basic linear operators and compositions of them. These are the free space propagation and the lens operator. In developing the wave optics simulation this principle has been kept, and two operators have been defined: propagation and lens. four different types of propagation operator have been described and compared. In analogy with ray tracing an optical system has been simulated using composition of the

two simple operators. In developing this platform all the media composing the system has been considered as linear, isotropic, homogeneous and non dispersive. The meaning of this properties in the following section

## 2.2 Scalar Theory of diffraction

The term diffraction has been defined by Sommerfeld as "any deviation of light rays from rectilinear paths which cannot be interpreted as reflection or refraction" [46]. The commplex vectorial equations describing wave propagation in three dimentional space can be simplified into a set of scalar equations using the Scalar Theory of Diffraction as expplained by Goodman [47]. The starting point is given by Maxwell Equations in absence of sources of electrical field of magnetic dipoles:

$$\begin{aligned} \nabla \times \vec{E} &= -\mu \frac{\partial \vec{H}}{\partial t} \\ \nabla \times \vec{H} &= \epsilon \frac{\partial \vec{E}}{\partial t} \\ \nabla \cdot \epsilon \vec{E} &= 0 \\ \nabla \cdot \mu \vec{B} &= 0 \end{aligned} \tag{2.1}$$

where  $\vec{E}$  is the electric field,  $\vec{H}$  is the magnetic field,  $\mu$  and  $\epsilon$  are respectively the magnetic permeability and electrical permittivity of the medium in which the optical wave is propagating. Both  $\vec{E}$  and  $\vec{H}$  are a functions of the position  $x, y$  and  $z$ , as well as the time  $t$ .

The operator  $\nabla$  is defined as:

$$\nabla = \frac{\partial}{\partial x} \hat{i} + \frac{\partial}{\partial y} \hat{j} + \frac{\partial}{\partial z} \hat{k} \quad (2.2)$$

where  $\hat{i}, \hat{j}$  and  $\hat{k}$  are unit vectors along directions  $x, y$  and  $z$ .

Propagation is assumed to happen in a dielectric medium that is linear, isotropic and homogeneous. A medium is linear if its response to a several disturbances acting simultaneously can be decomposed into the sum of the responses to the single disturbances taken individually. It is isotropic if its properties do not depends on the directions of polarization of the wave and is homogeneous if its permittivity is constant along all direction of propagation. The medium is considered also to be non dispersive, that is the permittivity  $\epsilon$  is not dependent on the wavelength.

Applying the operator  $\nabla \times$  to the left and to the right side of the first equation of 2.1 and using the vector identity

$$\nabla \times (\nabla \times \vec{E}) = \nabla(\nabla \cdot \vec{E}) - \nabla^2 \vec{E} \quad (2.3)$$

$$\nabla(\nabla \cdot \vec{E}) - \nabla^2 \vec{E} = \nabla \times (-\mu \frac{\partial \vec{H}}{\partial t}) \quad (2.4)$$

From the third equation in 2.1:

$$\nabla \cdot \epsilon \vec{E} = 0 \quad (2.5)$$

hence equation 2.4 becomes:

$$-\nabla^2 \vec{E} = \nabla \times (-\mu \frac{\partial \vec{H}}{\partial t}) \quad (2.6)$$

since both the operators  $\nabla \times$  and its derivative are linear it is possible to swap them on the right hand side of equation 2.4. Then substituting the second

Maxwell equation 2.1 into the 2.6:

$$-\nabla^2 \vec{E} = -\mu\epsilon \frac{\partial^2}{\partial t^2} \vec{E} \quad (2.7)$$

Where  $\nabla^2$  is the Laplacian operator defined as:

$$\nabla^2 = \frac{\partial^2}{\partial x^2} \hat{i} + \frac{\partial^2}{\partial y^2} \hat{j} + \frac{\partial^2}{\partial z^2} \hat{k} \quad (2.8)$$

We define the refractive index of the medium in which the wave is propagating as:

$$n = \sqrt{\frac{\epsilon\mu}{\epsilon_0\mu_0}} \quad (2.9)$$

where  $\epsilon_0$  is the permittivity of the vacuum and  $\mu_0$  the magnetic permeability in vacuum. Therefore the speed of light in the vacuum is:

$$c = \sqrt{\frac{1}{\epsilon_0\mu_0}} \quad (2.10)$$

Then the wave equation for the electric field becomes:

$$\nabla^2 \vec{E} - \frac{n^2}{c^2} \frac{\partial^2 \vec{E}}{\partial t^2} = 0 \quad (2.11)$$

Similar considerations can be done for the magnetic field, leading to an identical equation:

$$\nabla^2 \vec{H} - \frac{n^2}{c^2} \frac{\partial^2 \vec{H}}{\partial t^2} = 0 \quad (2.12)$$

Since the wave equation is obeyed by both the electric field and magnetic fields, it is possible to define a scalar wave equation, obeyed by the single components of those vectors. The scalar field components are represented as a function  $u(x, y, z, t)$  called field disturbance. The scalar wave equation is then:

$$\nabla^2 u - \frac{n^2}{c^2} \frac{\partial^2 u}{\partial t^2} = 0 \quad (2.13)$$

With this scalar approximation it is possible to treat the propagation of an optical field as a scalar. This is only valid under the assumption of a linear, isotropic, homogeneous and non dispersive medium, since all the component in all the directions of the electric and magnetic fields must behave identically.

### 2.2.1 Helmholtz equation

In the case of monochromatic wave the scalar field  $u$  is a function of time  $t$  and position  $\vec{X}$  defined as:

$$u(\vec{X}, t) = A(\vec{X}) \cos[2\pi\nu t - \phi(\vec{X})] \quad (2.14)$$

$A(\vec{X})$  is the amplitude of the disturbance and  $\phi(\vec{X})$  is its phase at point in the space with coordinates  $\vec{X} = (x, y, z)$ . Separating space and time dependence:

$$u(\vec{X}, t) = \operatorname{Re}\{U(\vec{X})e^{-j2\pi\nu t}\} \quad (2.15)$$

where  $U$  is a complex function of position and includes the a phase term  $e^{j\phi(\vec{X})}$ .

$$U(\vec{X}) = A(\vec{X})e^{j\phi(\vec{X})} \quad (2.16)$$

This field should satisfies the scalar wave equation 2.13. Substituting equation 2.16 into 2.13:

$$\nabla^2[U(\vec{X})e^{-j2\pi\nu t}] - \frac{n^2}{c^2} \frac{\partial^2}{\partial t^2}[U(\vec{X})e^{-j2\pi\nu t}] = 0 \quad (2.17)$$

Expressing the derivatives and simplifying the exponential terms:

$$\nabla^2[U(\vec{X})] + \left(\frac{2\pi\nu n}{c}\right)^2 [U(\vec{X})] = 0 \quad (2.18)$$

The wave number is defined as:

$$k = \frac{2\pi\nu n}{c} \quad (2.19)$$

and expression 2.18 becomes:

$$(\nabla^2 + k^2)U = 0 \quad (2.20)$$

Equation 2.20 is the Helmholtz equation and it describes the behaviour of a complex disturbance propagating in a homogeneous medium.

### 2.2.2 Solutions of Helmholtz Equations

An analytical expression of the complex disturbance  $U$  that satisfies the Helmholtz equation can be found using the green's theorem under particular boundaries condition as explained by Goodman [47]. There are two possible solutions: Fresnel-Kirchhoff and Rayleigh-Sommerfeld. Considering a wave  $U_0$  propagating through a diffracting screen at a point in space with coordinates  $z = 0$  with an aperture  $D$  the boundaries conditions:

- Fresnel-Kirchhoff (FK) conditions

$$U(x, y, 0) = U_0(x, y, 0) \text{ for } (x, y) \in D$$

$$U(x, y, 0) = 0 \text{ for } (x, y) \notin D$$

$$\frac{\partial U}{\partial z} = \frac{\partial U_0}{\partial z} \text{ for } (x, y) \in D$$

$$\frac{\partial U}{\partial z} = 0 \text{ for } (x, y) \notin D$$

- Rayleigh-Sommerfeld (RS) conditions:

$$U(x, y, 0) = U_0(x, y, 0) \text{ for } (x, y) \in D$$

$$U(x, y, 0) = 0 \text{ for } (x, y) \notin D$$

The FK conditions lead to a simple result but they are not physically correct since they imply the field after the screen to be zero outside of the aperture in the immediate proximity of the screen as well as its normal derivative. Results given by the FK condition are accurate only for a distance from the aperture much larger than the wavelength. The RS condition on the other hand is less strict since it does not require the derivatives of the disturbance and leads to a solution of the Helmholtz equation that is:

$$U(x, y, z) = \frac{1}{j\lambda} \iint_{\sigma} U(\xi, \eta, 0) \frac{e^{jkr}}{r} \cos(\theta) d\xi d\eta \quad (2.21)$$

where, with reference to figure 2.1,  $\theta$  is the angle between the  $z$  axis and the direction of propagation,  $r = \sqrt{z^2 + (x - \xi)^2 + (y - \eta)^2}$  is the distance between the point  $P_1 = (x, y, z)$  and  $P_0 = (\xi, \eta, 0)$  and  $\sigma$  is the area of aperture. Since  $\cos(\theta) = \frac{z}{r}$ :

$$U(x, y, z) = \frac{z}{j\lambda} \int \int_{\sigma} U(\xi, \eta, 0) \frac{e^{jkr}}{r^2} d\xi d\eta \quad (2.22)$$

Equation 2.22 is the Rayleigh-Sommerfeld diffraction formula [47], and can be simplified under the Fresnel approximation, as will be explained in section 2.2.3.

### 2.2.3 The Fresnel Approximation

It is possible to approximate the distance of propagation  $r$  between  $P_0$  and  $P_1$  with its Taylor expansion up to the second order:

$$r = \sqrt{1 + \left(\frac{x - \xi}{z}\right)^2 + \left(\frac{y - \eta}{z}\right)^2} \approx z \left[ 1 + \frac{(1)}{2} \left(\frac{x - \xi}{z}\right)^2 + \frac{1}{2} \left(\frac{y - \eta}{z}\right)^2 \right] \quad (2.23)$$

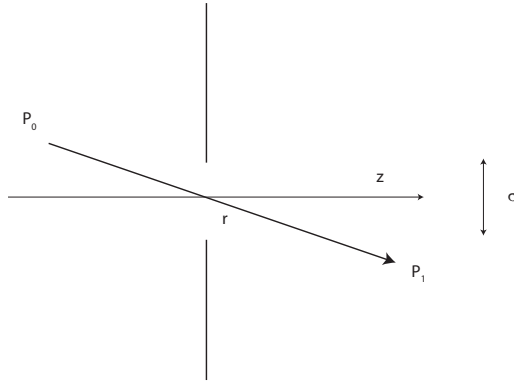


Figure 2.1: example

Therefore for large propagation distances,  $z \gg x, y$ , the diffraction integral becomes:

$$U(x, y) = \frac{e^{jkz}}{j\lambda z} \int \int_{-\infty}^{\infty} U(\xi, \eta) e^{\frac{jk}{2z}[(x-\xi)^2 + (y-\eta)^2]} d\xi d\eta \quad (2.24)$$

Factorizing the exponential term the disturbance becomes:

$$U(x, y) = \frac{e^{jkz}}{j\lambda z} e^{j\frac{k}{2z}(x^2+y^2)} \int \int_{-\infty}^{\infty} U(\xi, \eta) e^{\frac{jk}{2z}(\xi^2+\eta^2)} e^{\frac{-jk}{2z}(x\xi+y\eta)} d\xi d\eta \quad (2.25)$$

This can be seen as the Fourier transform of the disturbance before the aperture  $U(\xi, \eta)$  multiplied by a quadratic phase factor  $e^{\frac{jk}{2z}(\xi^2+\eta^2)}$  [47].

## 2.3 Operator Free space propagation: Fresnel Approximation approach

The first version of the operator free space propagation has been developed using the Fresnel Integral as written in equation 2.25. The input disturbance  $U(\xi, \eta)$  is considered to be illuminated by monochromatic light with wavelength  $\lambda$ . As stated in section 2.2.3 the Fresnel integral can be seen as the two dimensional Fourier transform of the input field  $U(\xi, \eta)$  multiplied

by a quadratic phase factor [47, 48]. This is going to be very useful from a computational point of view since it can be implemented with a fast Fourier transform algorithm (FFT) [49].

We define the function  $U'(\xi, \eta)$  as:

$$U'(\xi, \eta) = U(\xi, \eta) e^{\frac{jk}{2z}(\xi^2 + \eta^2)} \quad (2.26)$$

The optical field at the plane  $z$  is the product of the Fourier transform of  $U'(\xi, \eta)$  with the phase term  $e^{\frac{jk}{2z}(x^2 + y^2)}$ :

$$U(x, y) = \frac{e^{ikz}}{i\lambda z} e^{\frac{ik}{2z}(x^2 + y^2)} \mathcal{F}[U'(\xi, \eta)] \quad (2.27)$$

where the spatial frequencies of the Fourier Transform can be correlated with the spatial coordinates  $x$  and  $y$  by the relation:

$$\begin{cases} \nu_x = \frac{x}{\lambda z} \\ \nu_y = \frac{y}{\lambda z} \end{cases} \quad (2.28)$$

This method is computationally fast since it requires only one Fourier transform, and it is analytically correct. Particular attention should be given to the sampling of the optical field  $U$  and  $U'$ . Because of the presence of the Fourier transform the coordinates of the input and output fields are not sampled in the same way, but are scaled of a factor that is proportional to the distance of propagation, as shown in equation 2.28 [49]. Therefore the input and output planes have different sampling [48]. In addition the multiplicative phase factor:

$$e^{\frac{ik}{2z}(\xi^2 + \eta^2)} \quad (2.29)$$

presents to rapid oscillation of the phase of the optical field for small variations of  $z$ , since  $z$  is at its denominator [48, 50]. In order to avoid aliasing the

input field requires a large sampling and this is achieved by zero padding the sampling window of the input field, with an increase of the digital resolution of the field. It is known that the computational effort of the FFT algorithm increases with the resolution as  $O(n \log n)$ , where  $n$  is the number of samples of the input field and increasing the sampling resolution of the field leads to long a computational time.

### 2.3.1 Multi-Step Fresnel propagation operator

To overcome the scaling of the field and the large computational time required by the Fresnel propagation integral method, a modified method has been developed. We uses a multi step approach as the one explained by Sypek *et al.* [48, 51] and as its shown in figure 2.2 . The reason to adopt the multi-

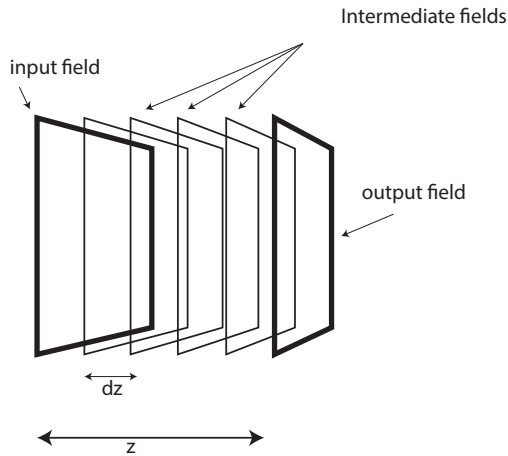


Figure 2.2: To remove the scaling factor between the input and output fields, a multi step Fresnel approach has been developed. The field is propagated by unit of  $dz$ , the minimum distance to keep the sampling the same.

step approach in this project is to remove the scaling factor between the input field and the output field that arise from the Fourier transform as shown in

equation 2.28, while Sypek developed a multi step propagation model to minimize the oscillations of the Fourier spectrum and to avoid large zero paddings.

In the Fourier domain, an optical field sampled by a  $N \times N$  pixels window, and with squared pixels that are  $dx$  wide the spatial frequency resolution is:

$$d\nu = \frac{1}{Ndx} \quad (2.30)$$

Therefore the pixel size in the image plane is according to equations 2.28:

$$d\xi = d\nu\lambda z \quad (2.31)$$

where  $z$  is the propagation distance and  $\lambda$  is the wavelength of the monochromatic wave. The condition to keep the same resolution both in the input field and the output field is:

$$d\xi = d\nu\lambda z = dx \quad (2.32)$$

Substituting the 2.30 into the 2.28:

$$\frac{1}{Ndx} = \frac{dx}{\lambda z} \quad (2.33)$$

Then resolving for  $z$  the minimum propagation distance  $dz$  to keep the same sampling both in the input and output fields is:

$$dz = \frac{W^2}{N\lambda} \quad (2.34)$$

and:

$$z = \sum_{i=1}^N dz_i \quad (2.35)$$

$W = Ndx$  is the dimension in meters of the input field. Equation 2.34 gives the length of the single step in which the propagation distance  $z$  should be

## 2.4. OPERATOR FREE SPACE PROPAGATION: ANGULAR SPECTRUM OF PLANE WAVES APPROACH

divided in order to keep the same resolution.

Although the results obtained with this multi-step approach are correct there are some issues. The propagation distance should be a multiple of  $dz$ , and this is a very significant limitation to the propagation distances that can be set in simulations. In plenoptic imaging systems it is important to know and set the propagation distances with extreme precision and any limitations is not acceptable. Another issue regards the computational time. With the multi step approach the number of FFT performed increases with the steps, leading to a computational time  $N$  times larger than the Fresnel Integral method. For these reasons the angular spectrum method as will be discussed in section 2.4 has been adopted in all the simulations presented in this work.

### 2.4 Operator Free space propagation: Angular spectrum of plane waves approach

The operator free space propagation can be derived considering the is proportional propagation distance [47]. In the Fourier domain the input disturbance can be seen as formed by a set of plane waves travelling in different directions, the *Angular Spectrum of Plane waves* representation of an optical field. In the next section the operator propagation as and its characteristic transfer function will be defined. Three versions of the angular spectrum operator will be presented, and performances of the three versions will be compared.

#### 2.4.1 Angular spectrum of plane waves

The disturbance  $U(x, y; 0)$  describing a monochromatic wave incident a plane  $(x, y)$  at the coordinate  $z=0$  while travelling along the z direction has a Fourier

transform given by:

$$A(f_x, f_y; 0) = \iint_{-\infty}^{\infty} U(x, y; 0) e^{-j2\pi(f_x x + f_y y)} dx dy \quad (2.36)$$

and  $U(x, y; 0)$  is equal to the inverse Fourier transform of its spectrum:

$$U(x, y; 0) = \iint_{-\infty}^{\infty} A(f_x, f_y; 0) e^{j2\pi(f_x x + f_y y)} df_x df_y \quad (2.37)$$

The physical meaning of the equation 2.37 is that the disturbance  $U(x, y; 0)$  can be decomposed in the sum of elemental plane waves propagating in directions given by the wave vector  $\vec{k}$  whose magnitude is  $2\pi/\lambda$  and direction is given by its direction cosines  $(\alpha, \beta, \gamma)$  [47, 50]. Dropping the temporal dependence the plane wave is then:

$$p(x, y, z) = e^{-j\vec{k} \cdot \vec{r}} \quad (2.38)$$

where

$$\vec{r} = x\hat{i} + y\hat{j} + z\hat{k} \quad (2.39)$$

and

$$\vec{k} = \frac{2\pi}{\lambda}(\alpha\hat{i} + \beta\hat{j} + \gamma\hat{k}) \quad (2.40)$$

The exponential becomes:

$$p(x, y, z) = e^{-j\frac{2\pi}{\lambda}(\alpha x + \beta y)} e^{-j\frac{2\pi}{\lambda}(\gamma z)} \quad (2.41)$$

The terms,  $\alpha, \beta$  and  $\gamma$  are the direction cosines of the wave vector  $\vec{k}$  and they are related as:

$$\gamma = \sqrt{1 - \alpha^2 + \beta^2} \quad (2.42)$$

Therefore the complex exponential function in equation 2.36 can be seen as a plane wave with direction cosines

$$\alpha = \lambda f_x, \quad \beta = \lambda f_y, \quad \gamma = \sqrt{1 - (\lambda f_x)^2 + (\lambda f_y)^2} \quad (2.43)$$

## 2.4. OPERATOR FREE SPACE PROPAGATION: ANGULAR SPECTRUM OF PLANE WAVES A

The angular spectrum of plane waves of the disturbance  $U(x, y : 0)$  is the function:

$$A\left(\frac{\alpha}{\lambda}, \frac{\beta}{\lambda}; 0\right) = \iint_{-\infty}^{\infty} U(x, y; 0) e^{-j2\pi(\frac{\alpha}{\lambda}x + \frac{\beta}{\lambda}y)} dx dy \quad (2.44)$$

After a prorogation of  $z$  the disturbance  $U(x, y; z)$  can be written in the form of the angular spectrum in analogy with equation 2.37:

$$U(x, y; z) = \iint_{-\infty}^{\infty} A(f_x, f_y; z) e^{j2\pi(f_x x + f_y y)} df_x df_y \quad (2.45)$$

where  $f_x = \alpha/\lambda$  and  $f_y = \beta/\lambda$ . To be a propagative disturbance, equation 2.45 should satisfy Helmholtz equation 2.20:

$$(\nabla^2 + k^2)U = 0 \quad (2.46)$$

Substituting equation 2.45 into 2.46:

$$\frac{d^2}{dz^2} A(f_x, f_y, z) + \left(\frac{2\pi}{\lambda}\right) [1 - (\lambda f_x)^2 + (\lambda f_y)^2] A(f_x, f_y, z) = 0 \quad (2.47)$$

A solution of the differential equation 2.47 is:

$$A(f_x, f_y, z) = A(f_x, f_y, 0) e^{j\frac{2\pi}{\lambda} \sqrt{1 - (\lambda f_x)^2 + (\lambda f_y)^2}} \quad (2.48)$$

The propagative solution is the one where the spatial frequencies satisfy the condition:

$$(\lambda f_x)^2 + (\lambda f_y)^2 < 1 \quad (2.49)$$

in this case the exponential term in equation 2.48 remains complex and the wave can propagate since it is an oscillating term. For the values of spatial frequencies that satisfy the condition:

$$(\lambda f_x)^2 + (\lambda f_y)^2 > 1 \quad (2.50)$$

the exponent in the equation 2.48 becomes real, and the exponential is a decay term. The solution is no longer propagative and waves are called evanescent waves. It is interesting to see how the angular spectrum theory is more complete than the Fresnel approximation since it includes evanescent components too.

Finally, the disturbance after a propagation in  $z$  can be expressed as a function of the disturbance  $U(x, y; 0)$  at the plane  $z=0$ :

$$U(x, y; z) = \int \int_{-\infty}^{\infty} A(f_x, f_y, 0) e^{j \frac{2\pi}{\lambda} \sqrt{1 - (\lambda f_x)^2 - (\lambda f_y)^2}} e^{j 2\pi (f_x x + f_y y)} df_x df_y \quad (2.51)$$

The last equation enables a calculation of the output field  $U(x, y; z)$  in terms of the input field and the propagation distance, under the approximation of a linear, isotropic, homogeneous and non dispersive medium.

Because of the linearity of the problem, the propagation is considered as a linear system that maps the input disturbance  $U(x, y; 0)$  into the a new field distribution  $U(x, y; z)$ [47]. This linear system is characterized by a transfer function whose bandwidth is limited to the case of the propagative solution of equation 2.47, excluding the evanescent waves. The angular spectrum of the output field can be rewritten as the product of the angular spectrum of the input field multiplied by the transfer function  $H(f_x, f_y)$ :

$$A(f_x, f_y; z) = A(f_x, f_y; 0) \cdot H(f_x, f_y; z) \quad (2.52)$$

The propagation is fully described by the transfer function:

$$H(f_x, f_y) = \begin{cases} e^{j \frac{2\pi z}{\lambda} \sqrt{1 - (\lambda f_x)^2 - (\lambda f_y)^2}} & \text{if } \sqrt{f_x^2 + f_y^2} < \frac{1}{\lambda} \\ 0 & \text{otherwise} \end{cases} \quad (2.53)$$

The bandwidth can be represented as a circle in Fourier space. For frequencies smaller than  $1/\lambda$  the transfer function introduces a shift in the spatial

## 2.4. OPERATOR FREE SPACE PROPAGATION: ANGULAR SPECTRUM OF PLANE WAVES A

domain that is responsible for diffraction [47]. Results obtained with the angular spectrum method are similar to the ones obtained with the Fresnel approximation, but no scaling factor between the input and output field is introduced. From a computational point of view, the angular spectrum operator is composed by 3 steps:

1. Fourier transform of the input field
2. Multiplication of the Fourier transform of the input field with the propagation transfer function in equation 2.53
3. Inverse Fourier transform of the product at step 2. The resultant field is the output disturbance after the propagation in free space.

The process can be seen in figure 2.3

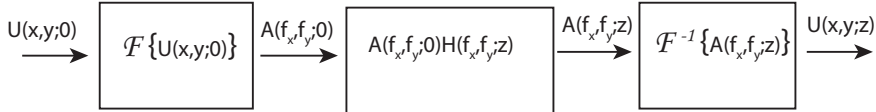


Figure 2.3: Structure of the operator free space propagation with the angular spectrum of plane waves method. The initial disturbance  $U(x, y; 0)$  is transformed into the angular spectrum  $A(f_x, f_y; 0)$  with a Fourier transform implemented by a FFT algorithm. The angular spectrum is multiplied by the propagation transfer function  $H(f_x, f_y)$  and the resultant angular spectrum is inverse transformed into the output disturbance  $U(x, y; z)$

### 2.4.2 Band Limited Angular Spectrum

The transfer function of the propagation in equation 2.53 is a complex exponential oscillating with a frequency depending by the propagation distance  $z$ . Figure 2.4 shows four different profiles of the transfer function for four

propagation distances,  $1\text{ mm}$ ,  $2\text{ mm}$ ,  $10\text{ mm}$  and  $20\text{ mm}$ . Aliasing effects are evident since even for a propagation distance of  $2\text{ mm}$ . When the  $z$  becomes large, the aliasing arises at low spatial frequencies, narrowing the useful bandwidth of the transfer function [50].

## 2.4. OPERATOR FREE SPACE PROPAGATION: ANGULAR SPECTRUM OF PLANE WAVES A

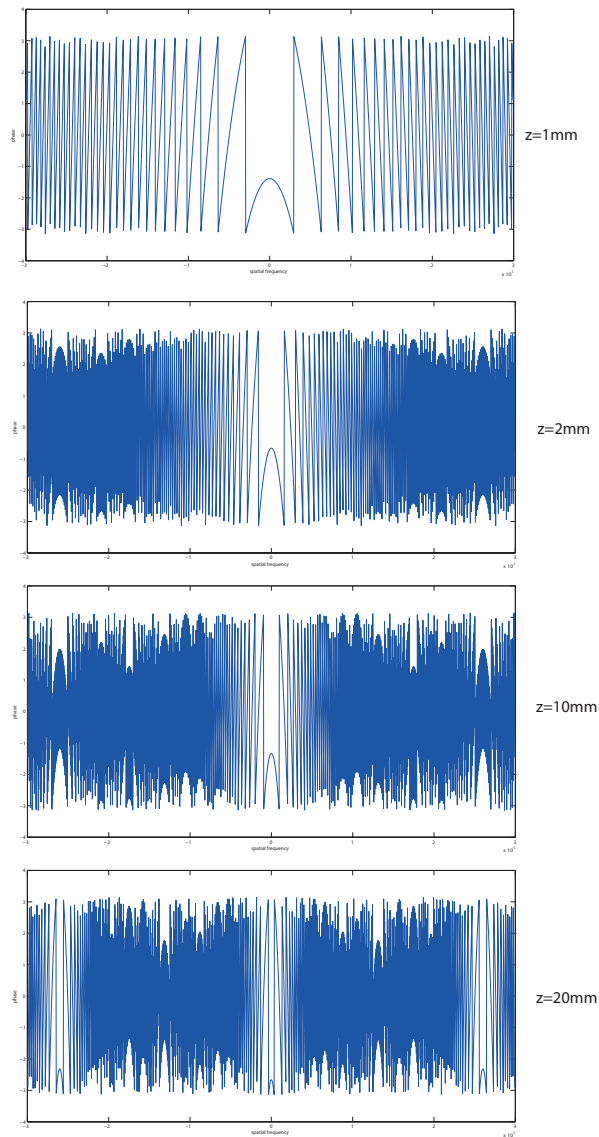


Figure 2.4: Cross section along of the phase of the transfer function of the angular spectrum. It is evident how increasing the propagation distance the oscillation frequency become larger and aliasing arise.

The transfer function can be rewritten as:

$$H(f_x, f_y) = e^{j\phi(f_x, f_y)} \quad (2.54)$$

where  $\phi$  is the oscillating phase term as:

$$\phi(f_x, f_y) = \frac{2\pi}{\lambda} \sqrt{1 - \lambda f_x^2 - \lambda f_y^2} \quad (2.55)$$

Defining the local spatial frequencies of the transfer function [47, 50] as the frequency of the phase oscillation  $\nu_x$  and  $\nu_y$  along  $f_x$  and  $f_y$ :

$$\begin{cases} \nu_x = \frac{1}{2\pi} \frac{\partial}{\partial f_x} \phi(f_x, f_y) \\ \nu_y = \frac{1}{2\pi} \frac{\partial}{\partial f_y} \phi(f_x, f_y) \end{cases} \quad (2.56)$$

the local spatial frequencies become:

$$\begin{cases} \nu_x = -\frac{z}{\lambda} \frac{\lambda^2 f_x}{\sqrt{1 - (\lambda f_x)^2}} \\ \nu_y = -\frac{z}{\lambda} \frac{\lambda^2 f_y}{\sqrt{1 - (\lambda f_y)^2}} \end{cases} \quad (2.57)$$

As stated by Matsushima *et al.* [50], if the input optical disturbance is sampled by an  $N \times N$  sampling window with pixel size  $dx$ , the transfer function is sampled by unit of spatial frequency equals to  $df = 1/(Ndx)$ . To satisfy the Nyquist condition the sample frequency should be at least the double of the bandwidth of the transfer function. For one direction in the local frequency space:

$$\frac{1}{df} \geq 2|\nu_x| \quad (2.58)$$

Modifying the sampling of the transfer function, and of the input field, can lead to huge sampling windows and long computational times. In addition to that in practical applications the sampling interval is usually fixed. Therefore the condition on the maximum frequency range for which the transfer

## 2.4. OPERATOR FREE SPACE PROPAGATION: ANGULAR SPECTRUM OF PLANE WAVES A

function is not aliased:

$$\frac{1}{df_x} \geq 2z \frac{|f_x|}{|\sqrt{(\frac{1}{\lambda^2} + f_x)^2}|} \quad (2.59)$$

Resolving the equation for  $|f_x|$  :

$$|f_x| \leq \frac{1}{\sqrt{(2df_x z)^2 + 1\lambda}} = f_{max} \quad (2.60)$$

Where  $f_{max}$  is the maximum frequency of the transfer function without generating errors due to aliasing. Assuming the sampling of the optical field to be the same in both x and y direction the maximum bandwidth for the sampling in  $f_y$  is equal to the bandwidth in  $f_x$ . Therefore:

$$\frac{1}{df_y} \geq 2|\nu_y| \quad (2.61)$$

$$\frac{1}{df_y} \geq 2z \frac{|f_y|}{|\sqrt{\frac{1}{\lambda^2} + f_y)^2}|} \quad (2.62)$$

$$|f_y| \leq \frac{1}{\sqrt{(2df_y z)^2 + 1\lambda}} = f_{max} \quad (2.63)$$

To avoid aliasing then, the two dimensional transfer function should be limited to a range of frequencies defined by equation 2.62. The expression of the output field will then be:

$$U(x, y; z) = \mathcal{F}^{-1} [A(f_x, f_y; 0)H'(f_x, f_y; z)] \quad (2.64)$$

where

$$H_{BL}(f_x, f_y; z) = H(f_x, f_y; z) \text{rect} \left( \frac{f_x}{f_{max}} \right) \text{rect} \left( \frac{f_y}{f_{max}} \right) \quad (2.65)$$

The MATLAB algorithm to implement the band limitation consists in multiplying the phase term of the propagation transfer function by a phase mask

with the shape of a circle function of radius  $f_{max}$  in the plane of the spatial frequencies. A circular phase mask has been chosen instead of the rectangular phase mask of equation 2.65 because it follows the geometry of the lens aperture, without introducing new spatial features that could effect the diffraction.

The resultant phase of the transfer function is shown in figure 2.5, with the bandwidth for three different propagation distances.

## 2.4. OPERATOR FREE SPACE PROPAGATION: ANGULAR SPECTRUM OF PLANE WAVES A

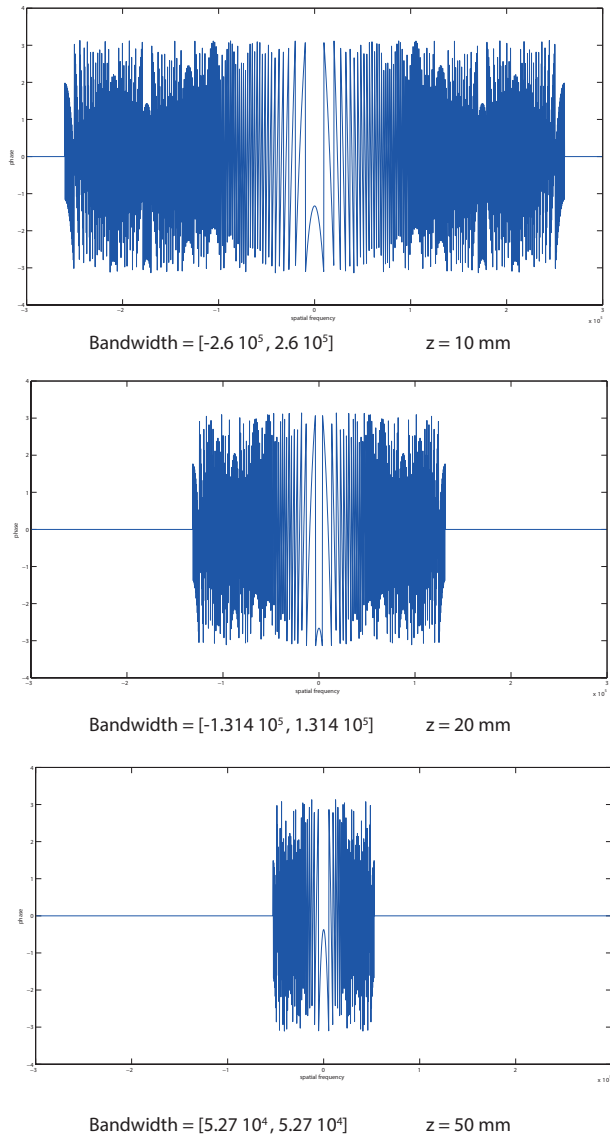


Figure 2.5: Bandwidth of the transfer function for three different propagation distances.

From a computational point of view the algorithm to implement the band limited angular spectrum method can be summarized in the following steps:

1. Computation of the angular spectrum of the input disturbance via a Fourier transform as shown in equation 2.37.

2. Estimation of the maximum bandwidth of the transfer function in order to avoid aliasing error using equations 2.60.
3. Multiplication of the phase of the transfer function for a circular phase mask with radius equal to the frequency obtained in the previous step.
4. Multiplication of the angular spectrum for the band limited transfer function.
5. Inverse Fourier transform of the product at step 4

The structure of the operator free space propagation implemented by the band limited angular spectrum can be seen in figure 2.6

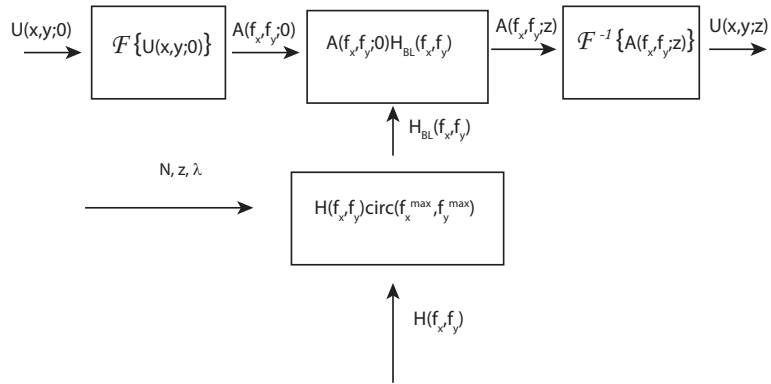


Figure 2.6: Structure of the operator free space propagation with the angular spectrum of plane waves method in its band limited version. The initial disturbance  $U(x, y; 0)$  is transformed into the angular spectrum  $A(f_x, f_y; 0)$  with a Fourier transform implemented by a FFT algorithm. The angular spectrum is multiplied by the propagation transfer function  $H(f_x, f_y)$  whose bandwidth has been limited according to equation 2.63. The bandwidth of the transfer function depends on the sampling of the input field, the wavelength of the light  $\lambda$  and the propagation distance. The resultant angular spectrum is inverse transformed into the output disturbance  $U(x, y; z)$ .  $N$  is the sampling of the input field,  $z$  the propagation distance and  $\lambda$  the wavelength.

### 2.4.3 Corrected Band Limited Angular Spectrum Method

The third method to implement the propagation operator with the angular spectrum is the corrected band limited angular spectrum method. It differs from the band limited angular spectrum presented in section 2.4.1 the bandwidth of the transfer function is truncated to the value of cut-off frequency of the free space propagation in case the Nyquist criterion requires a bandwidth too narrow. For long propagation distances the propagation transfer function acts as a low pass filter on the spatial frequency components of the input signal. When its bandwidth is bigger than the cutoff frequency calculated with the band limited method to avoid digital aliasing there is a loss of resolution in the final image. A trade-off should therefore be found between the error due to the aliasing and the error due to the excessive band limitation. For imaging applications this is not an issue since usually the numerical aperture of the optical elements in the imaging system give already a limitation in the band passing from the input field to the output field. However it is useful to estimate the bandwidth of the free space propagation defining the maximum spatial frequency that is transferred from the object plane to the image plane. This value defines the amount of information transferred from the input field to the image plane. With reference to figure 2.7 for a point in the input field, the range of spatial frequencies that are transferred to the output field are the ones whose direction cosines are contained into the angle that includes the sampling window of the output field. In the hypothesis of the propagation distance much bigger than the sampling window,  $z \gg W$  like in most of the applications of this simulation toolbox the angle  $\theta$  is equal

to:

$$\theta \simeq \frac{W}{z} \quad (2.66)$$

The link between the direction cosine and the spatial frequency is, according

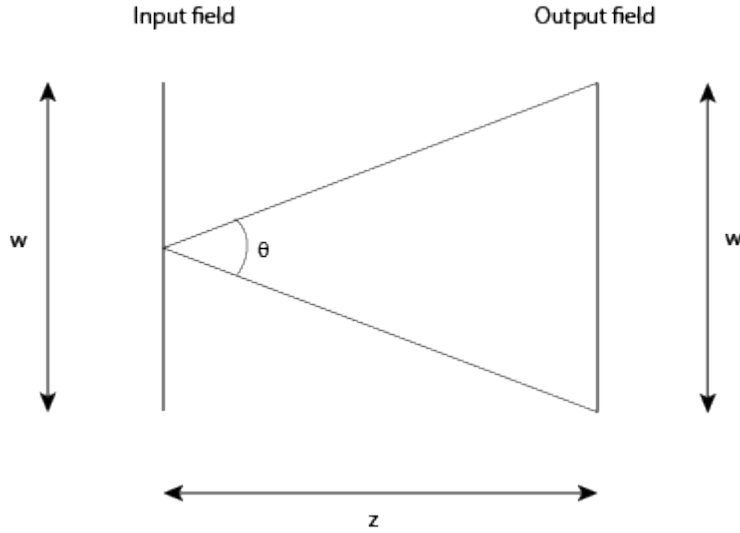


Figure 2.7: The maximum spatial frequency is linked to the dimension of the sampling window of the output field  $w$  and the propagation distance  $z$

to equation 2.43

$$\theta = \lambda f_{cutoff}, \quad (2.67)$$

The cutoff frequency of a field sampled by a sampling window  $W$  and after a propagation distance of  $z$  is defined as:

$$\nu_{cutoff} = \frac{W}{\lambda z} \quad (2.68)$$

Therefore the bandwidth of the transfer function should be bigger than  $\nu_{cutoff}$  in order not to introduce error in the reconstruction of the diffraction pattern due to loss in resolution.

$$f_{max} \geq \nu_{cutoff} \quad (2.69)$$

## 2.4. OPERATOR FREE SPACE PROPAGATION: ANGULAR SPECTRUM OF PLANE WAVES A

If the propagation distance limits the bandwidth of the output field too much, the transfer function can be improved by increasing the sampling of the input field. This condition is equal to having a smaller pixel size. Dealing with bigger sampling windows however increases the computational effort.

### 2.4.4 Performances of the Angular spectrum methods

To evaluate the differences in resolution of the three variants of the angular spectrum methods, Normal Angular spectrum (AS), Band Limited angular spectrum (BL), and Corrected Band Limited Angular Spectrum (corrected BL), it has been implemented a simulation of a free space propagation of an input field that consisted in a circular pupil of diameter 5 mm, sampled with a resolution of  $3000 \times 3000$  pixels with a sampling window of 1 cm. The propagation distances  $z$  varied from 1 m to 10 m. Results are shown in figure 2.8 where the cross section of the diffraction patterns are shown. The BL method shown in the central column gives smooth diffraction patterns. Increasing the propagation distance though the intensity profile lose part of the information because of the excessive low pass filtering action on the propagation transfer function, leading the the complete loss of the diffraction fringes. A comparison with the normal method (AS) can be seen in figure 2.8, where the diffraction fringes are presents with the superimposition of the noise due to aliasing in transfer function sampling. This affects the resolution of the diffraction pattern and the signal to noise ration drops with  $z$  as shown in figure 2.9. A good compromise is found using as bandwidth of the transfer function the one of the propagation obtained with the corrected BL method as explained in section 2.4.3 and as it is shown in figure 2.8 on the

far right column. fringes are clearly present in the diffraction pattern even for large propagation distances and the noise is removed. In figure figure 2.9 the signal to noise ratio (SNR) of the diffraction patterns in figure 2.8 is plotted as a function of the propagation distance for the three examined cases. The band limited angular spectrum method gives a better especially for short propagation distances, where the bandwidth of the transfer function is not low passing the signal but only avoiding the aliasing. It stays in general above the SNR of the corrected BL method, indicated in red of almost 15dB even in the case of large propagation distances. This is due to the excessive smoothing action that brings to the loss of resolution. On the other hand without any limitation of the band (AS), green line, the aliasing generated noise becomes dominant for long propagation distances and the SNR approach the 0 dB value. The best results in terms of resolution and noise reduction are given by the corrected BL method where the information on the diffraction is entirely kept.

## 2.4. OPERATOR FREE SPACE PROPAGATION: ANGULAR SPECTRUM OF PLANE WAVES A

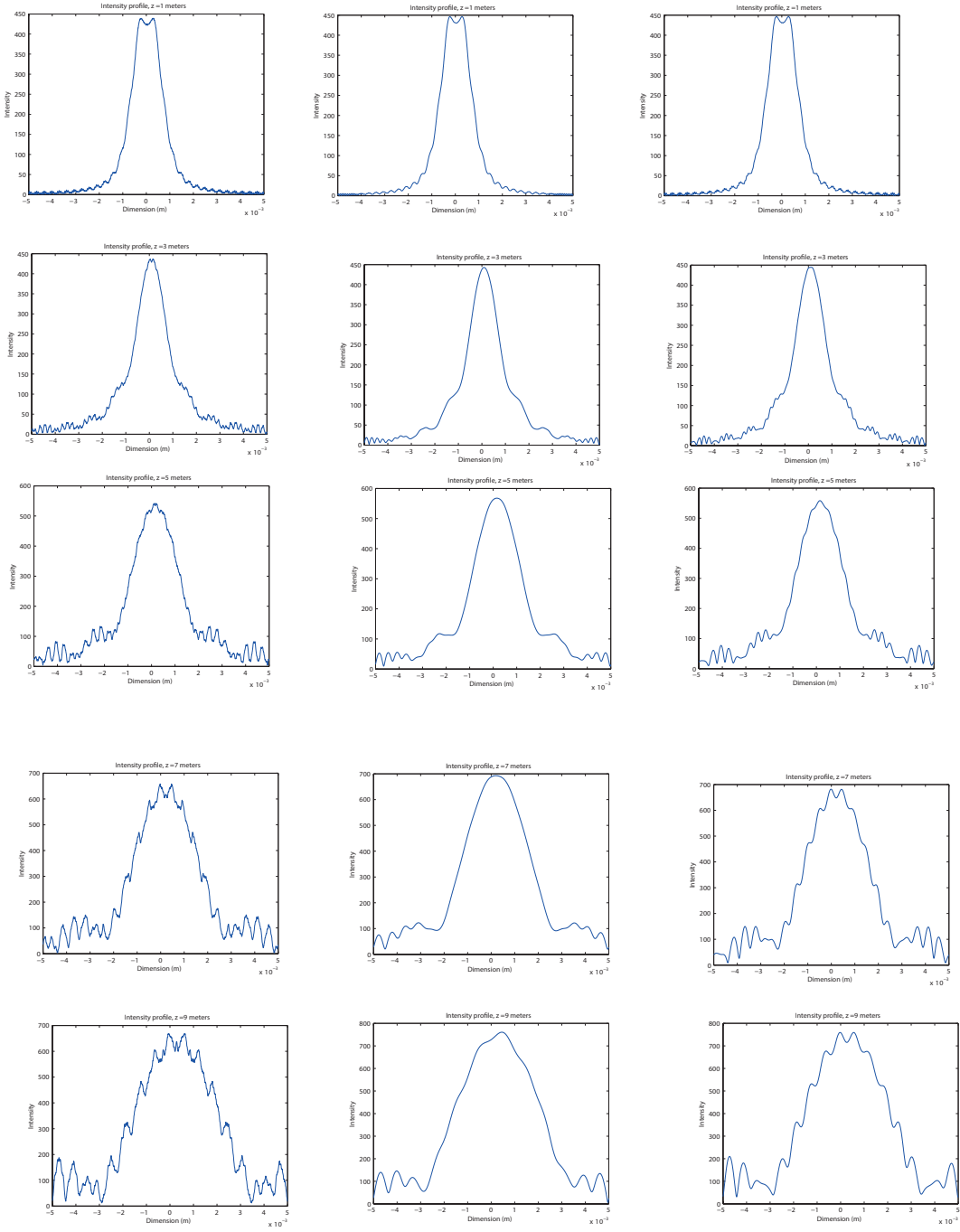


Figure 2.8: Comparison of the performances of the three angular spectrum propagation operator. On the left column are shown diffraction pattern cross section obtained using the angular spectrum method (AS). In the central column the pattern for the same propagation distances have been obtained using the band limited method (BL) and in the right column the same patterns have been obtained using the correct band limited method (corrected BL).

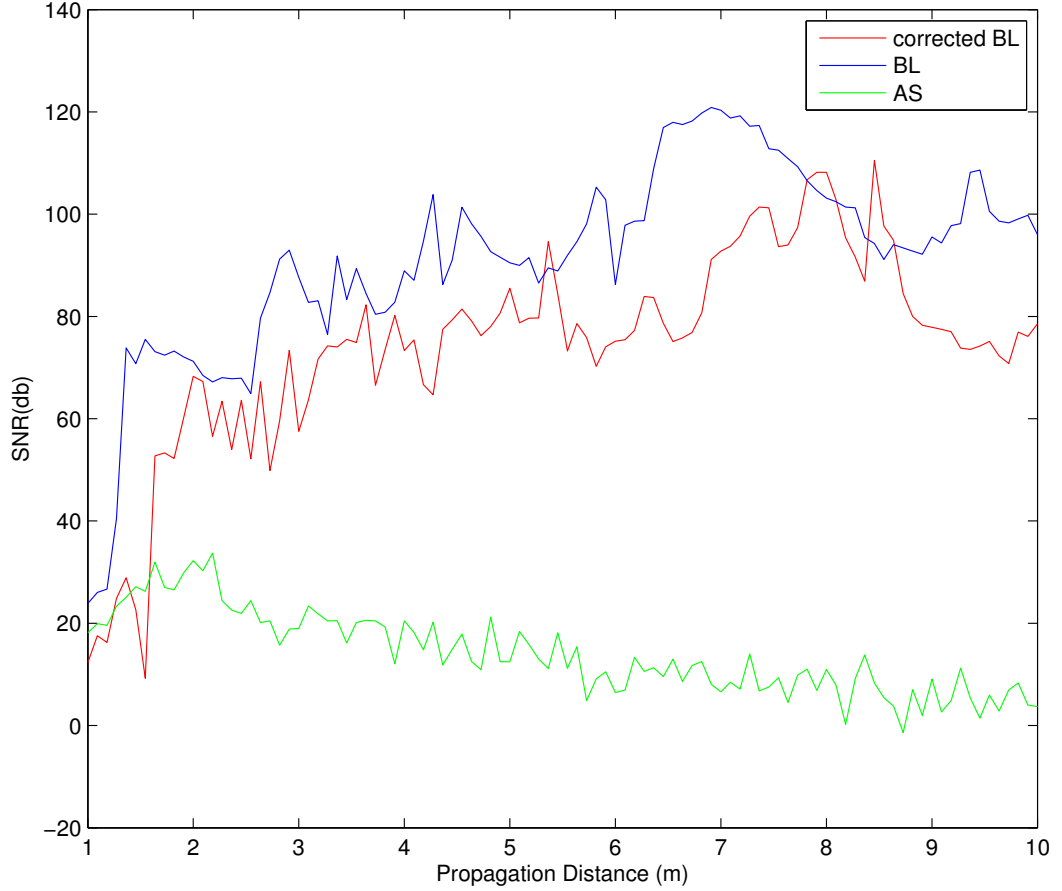


Figure 2.9: Comparison between the Signal to Noise ratio (SNR) as a function of the propagation distance for the three propagation method seen in section 2.4.1. The BL and the corrected BL methods improve the SNR, that instead drops with the increasing of the propagation distance when the normal AS method is used.

## 2.5 Operator Thin Lens

In this section will be described how the operator thin lens has been designed and implemented in the simulation toolbox. For the theory behind the main reference is Goodman [47]. A lens is composed of a material with a refractive

index different from the one of air, normally 1.5, that causes the propagation velocity of the optical field to drop. In the approximation of a thin lens, the translation of the ray of light inside the lens is negligible and if a ray enters the lens at the coordinate  $(x, y)$  on one face, it exits at the same coordinates at the other side. A thin lens delays an incident wave-front by an amount proportional to its thickness. These delays can be modelled introducing a phase factor to the incident field. The thickness function is:

$$\Delta(x, y) \quad (2.70)$$

as the thickness of the lens at the coordinates  $(x, y)$  as shown in figure 2.10, where  $\Delta_0$  is the lens maximum thickness at the coordinates  $(0, 0)$ . The phase

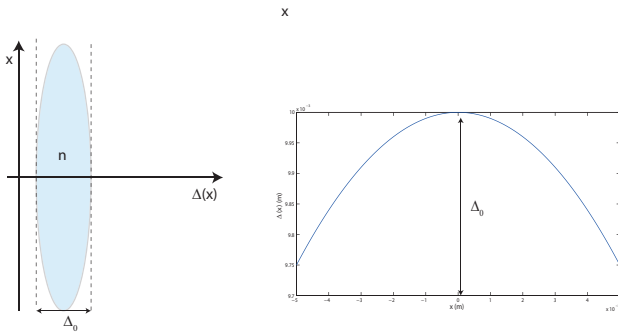


Figure 2.10: Thickness of a lens as a function of position along x coordinate. It can be defined in the same way along the y coordinate

delay introduced by the lens is proportional to its thickness:

$$\phi(x, y) = kn\Delta(x, y) + k[\Delta_0 - \Delta(x, y)] \quad (2.71)$$

where  $n$  is the refractive index of the lens material and  $k = 2\pi/\lambda$  is the wave number. With reference to figure 2.10 the quantity  $kn\Delta(x, y)$  is the phase

delay introduced by the different material of the lens, and  $k[\Delta_0 - \Delta(x, y)]$  is the phase delay introduced by the free space propagation between the two planes represented with dashed line. This phase delay can be seen as a multiplicative phase term defined as:

$$t_{lens} = \exp[jk\Delta_0] \exp[jk(n - 1)\Delta(x, y)] \quad (2.72)$$

The complex field  $U'(x, y)$  immediately after the lens is therefore given by the product of the field entering the lens  $U_0(x, y)$  with the phase delay in equation 2.72.

$$U'(x, y) = t_{lens}(x, y)U_0(x, y) \quad (2.73)$$

The sign convention used in the following derivation is: for a ray of light travelling from left to right:

- any convex surface encountered has positive radius of curvature
- any concave surface encountered had negative radius of curvature

The lens can be split into three elements such that the total thickness function is the sum of three functions: From figure 2.11:

$$\Delta(x, y) = \Delta_1(x, y) + \Delta_2(x, y) + \Delta_3(x, y) \quad (2.74)$$

Where the three components of the thickness are:

$$\Delta_1(x, y) = \Delta_{01}(x, y) - R_1 \left(1 - \sqrt{1 - \frac{x^2 + y^2}{R_1^2}}\right) \quad (2.75)$$

$$\Delta_2(x, y) = \Delta_{02} \quad (2.76)$$

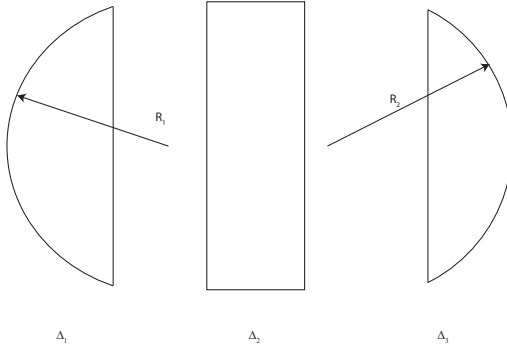


Figure 2.11: The thickness function can be decomposed into the sum of three contributions.

$$\Delta_3(x, y) = \Delta_0(x, y) - R_2 \left( 1 - \sqrt{1 - \frac{x^2 + y^2}{R_2^2}} \right) \quad (2.77)$$

$R_1 > 0$  and  $R_2 < 0$  are respectively the radius of curvature of the right-hand surface and the radius of curvature of the left-hand side of the lens surface. Then total thickness function is given by:

$$\Delta(x, y) = \Delta_0(x, y) - R_1 \left( 1 - \sqrt{1 - \frac{x^2 + y^2}{R_1^2}} \right) + R_2 \left( 1 - \sqrt{1 - \frac{x^2 + y^2}{R_2^2}} \right) \quad (2.78)$$

where  $\Delta_0$  is:  $\Delta_0 = \Delta_{01} + \Delta_{02} + \Delta_{03}$ . In the paraxial approximation it is possible to approximate  $\Delta(x, y)$  with its first element of the Taylor series:

$$\sqrt{1 - \frac{x^2 + y^2}{R_1^2}} \approx 1 - \frac{x^2 + y^2}{R_1^2} \quad (2.79)$$

$$\sqrt{1 - \frac{x^2 + y^2}{R_2^2}} \approx 1 - \frac{x^2 + y^2}{R_2^2} \quad (2.80)$$

Substituting 2.79 and 2.80 into equation 2.78:

$$\Delta(x, y) = \Delta_0(x, y) - \frac{x^2 + y^2}{2} \left( \frac{1}{R_1} + \frac{1}{R_2} \right) \quad (2.81)$$

and substituting 2.81 into equation 2.71 the result is the expression of the phase shift in the exponential form:

$$t_l(x, y) = \exp[jkn\Delta_0] \exp[-jk(n-1) \frac{x^2 + y^2}{2} \left( \frac{1}{R_1} + \frac{1}{R_2} \right)] \quad (2.82)$$

The focal length of the lens  $f$  is the quantity containing the information on the physical properties of the lens and it is defined as:

$$\frac{1}{f} \equiv (n-1) \left( \frac{1}{R_1} + \frac{1}{R_2} \right) \quad (2.83)$$

Finally after dropping the constant phase factor the effects of a thin lens under par-axial approximation as a quadratic phase transformation are described by equation 2.84:

$$t_l(x, y) = \exp[-j \frac{k}{2f} (x^2 + y^2)] \quad (2.84)$$

This equation can represent the effects of any lens, since the sign of  $f$  will define whether the lens is positive or negative. The physical meaning of this expression can be understood examining figure 2.12 When a plane wave, represented by the complex field  $U(x, y)$ , is normally incident on the lens, according to equation 2.73, the field coming out of the lens will be:

$$U'(x, y) = \exp[-j \frac{k}{2f} (x^2 + y^2)] \quad (2.85)$$

The thin lens is introducing a phase term on the incident field, and the resulting field is a quadratic approximation of a spherical wave. As shown

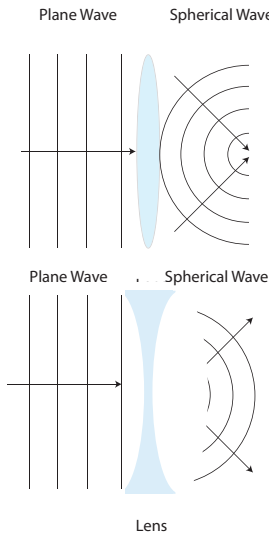


Figure 2.12: A thin lens converts a plane wave into a spherical wave.

in figure 2.12 when  $f$  is positive, the wave is converging towards a point on the optical axis at distance  $f$  from the lens. If  $f$  is negative the wave is diverging from a point on the optical axis placed at a distance  $|f|$  in front of the lens. The lens therefore transforms a plane wave into a spherical wave. The operator thin lens is defined as the product of the quadratic transformation in equation 2.84 with a function describing the aperture of the lens, called pupil  $P(x, y)$ :

$$L(x, y) = P(x, y) \exp[-j \frac{k}{2f} (x^2 + y^2)] \quad (2.86)$$

where the pupil function is defined as:

$$P(x, y) = \begin{cases} 1 & \sqrt{x^2 + y^2} < r \\ 0 & \text{elsewhere} \end{cases} \quad (2.87)$$

where  $r$  is the the radius of the lens aperture.

### 2.5.1 Aliasing in phase sampling

The quadratic phase factor of the thin lens operator is a complex function whose modulus is constant and equal to the unity, and its argument is an oscillating function in the interval  $(0, 2\pi]$ . The argument of the phase factor is shown in figure 2.13

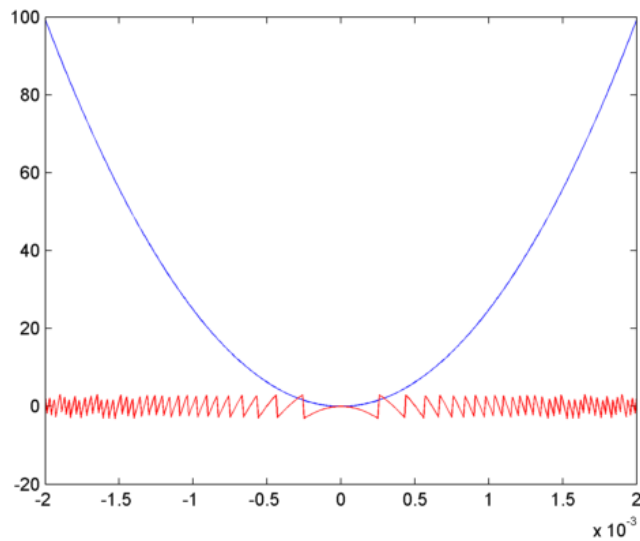


Figure 2.13: Phase profile of a computer generated lens. The blue line shows the quadratic phase term and the red line shows the same phase term wrapped every  $2\pi$ . This wrapping is the source of the aliasing.

The parabolic phase profile gets wrapped since the argument of a complex function varies between 0 and  $2\pi$ . This wrapping of the phase can cause aliasing as the distance from the centre of the lens increases. For high values of  $x$  and  $y$ , the quadratic term becomes too steep and the frequency of oscillation between 0 and  $2\pi$  of the phase factor might become too high to be correctly sampled. With analogy of what has been said in section 2.4, for

a parabolic phase profile:

$$\Phi(x, y) = \frac{k}{2f}(x^2 + y^2) \quad (2.88)$$

The instantaneous frequencies of the phase  $\nu_x$ ,  $\nu_y$  in  $x$  and  $y$  respectively are defined as:

$$\begin{cases} \nu_x = \frac{1}{2\pi} \frac{\partial \Phi}{\partial x} = \frac{1}{2\pi} \frac{k}{f} x \\ \nu_y = \frac{1}{2\pi} \frac{\partial \Phi}{\partial y} = \frac{1}{2\pi} \frac{k}{f} y \end{cases} \quad (2.89)$$

In order to recover all the components of a periodic signal, the sampling frequency should be at least twice the bandwidth of the signal. According to the Nyquist criterion:

$$f_{Nyquist} = 2\nu_{max} \quad (2.90)$$

The maximum instantaneous frequency  $\nu_{max}$  of the phase factor is the one that correspond to the edge of the lens. We consider for brevity the one dimensional case along the  $x$  direction, but the conclusions are valid for the  $y$  direction because of the rotational symmetry of the pupil function in equation 2.87. In this case  $x_{max} = y_{max} = r$  where  $r$  is the radius of the pupil function. Defining the pixel size  $\Delta x$  along  $x$ , and assuming the pixels as squared, so that the sampling frequency  $1/\Delta x$  is the same along both axis, the Nyquist condition to avoid aliasing is:

$$\frac{1}{\Delta x} \geq \frac{1}{2\pi} \frac{k}{f} x_{max} \quad (2.91)$$

Since in general the sampling rate cannot be modified because of the fixed pixel size of the sensor this expression leads to a condition for the radius of the pupil function:

$$r = x_{max} \leq \frac{2\pi f}{k \Delta x} \quad (2.92)$$

Substituting  $k = \frac{2\pi}{\lambda}$  into 2.92:

$$r \leq \frac{\lambda f}{\Delta x} \quad (2.93)$$

The more powerful is the lens,  $f$  will have a smaller value and hence the aperture should be smaller. Since the simulation platform is flexible, in case a particular value of the aperture is needed the equation 2.93, in order to get a condition on the focal length:

$$f \geq \frac{r \Delta x}{\lambda} \quad (2.94)$$

And considering that the digital resolution of a lens with aperture equal to  $2r$  is given by:

$$N = \frac{2r}{\Delta x} \quad (2.95)$$

The minimum resolution of a lens of radius  $r$  and focal length  $f$  is therefore:

$$N \geq \frac{2r^2}{f\lambda} \quad (2.96)$$

Applying these conditions will assure that no aliasing will be introduced by the lens operator.

## 2.6 Comparison between the free space propagation operators

In this section the differences in performance between the Fresnel approximation and the angular spectrum of plane waves approach will be shown, with particular attention to the computational time required by the different methods, the optical resolution and the error. Results will be used to evaluate the characteristic of the different propagation operators.

### 2.6.1 Description of the system

The system simulated is a simple imaging system composed of a single lens with focal length  $f = 158\text{mm}$ , in a  $2f$  configuration, as shown in figure 2.14. The field of view is a square of  $1\text{cm} \times 1\text{cm}$ , and the resolution of the input field is  $2000 \times 2000$  pixels. The aperture of the lens is  $D = 5\text{mm}$  and its f number, defined as:

$$F_{\#} = \frac{z}{D} \quad (2.97)$$

is equal to  $F_{\#} = 63$ , where  $z$  is the distance from the lens to the image plane, that in a  $2f$  configuration is equal to  $z = 2f = 316\text{mm}$ . The optical cut-off

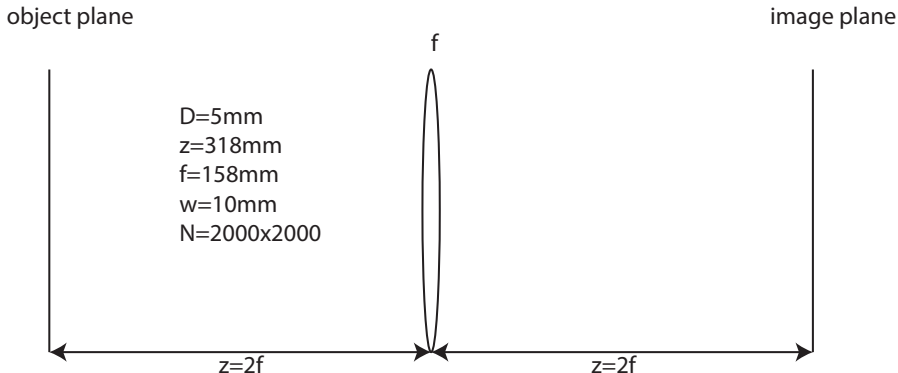


Figure 2.14: Schematic of the  $2f$  system simulated.  $f$  is the focal length,  $z$  the propagation distances,  $D$  is the aperture of the lens,  $w$  the field of view and  $N$  the sampling resolution.

frequency of this system is given by the relation [47]:

$$\nu_c = \frac{1}{\lambda F_{num}} \quad (2.98)$$

and for the system simulated, illuminated with monochromatic light with wavelength  $\lambda = 633\text{nm}$ , it is  $\nu_c = 2.5 \cdot 10^4 \text{cycles/m}$ .

### 2.6.2 Image of a point source

The first experiment simulated is the image of a point source, realized with a pinhole of  $10\mu m$  of diameter placed at the object plane indicated in figure 2.14. The image has been taken using four different methods to propagate the light into the system. Those are:

- Multi step Fresnel method (MSF), section 2.3.1
- Angular spectrum method (AS), section 2.4
- Band Limited Angular Spectrum method (BL), section 2.4.1
- corrected Band Limited Angular Spectrum method (cBL), section 2.4.3

Using as an input field a point source it will be computed the impulse response of each of these different methods. The sequence of operators used to simulate the system is shown in figure 2.15

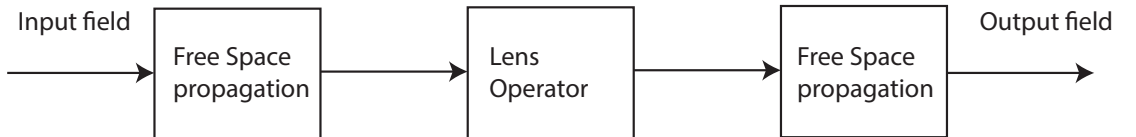


Figure 2.15: Operator sequence for the 2f system.

In the assumption of having a lens with a circular aperture and no aberrations, the impulse response of an optical system is an Airy Disk, that is the Fourier transform of the pupil of the system at the image plane. The fact that the theoretical output of the experiment is well known allows to determine the quality of the simulations tools. In addition to that, the Fourier

transform of the impulse response of an optical system gives information on the frequencies content of the image, hence the band pass of the imaging system and its quality. Figure 2.16 shows the sensor image at the image plane together with intensity profiles of the image.

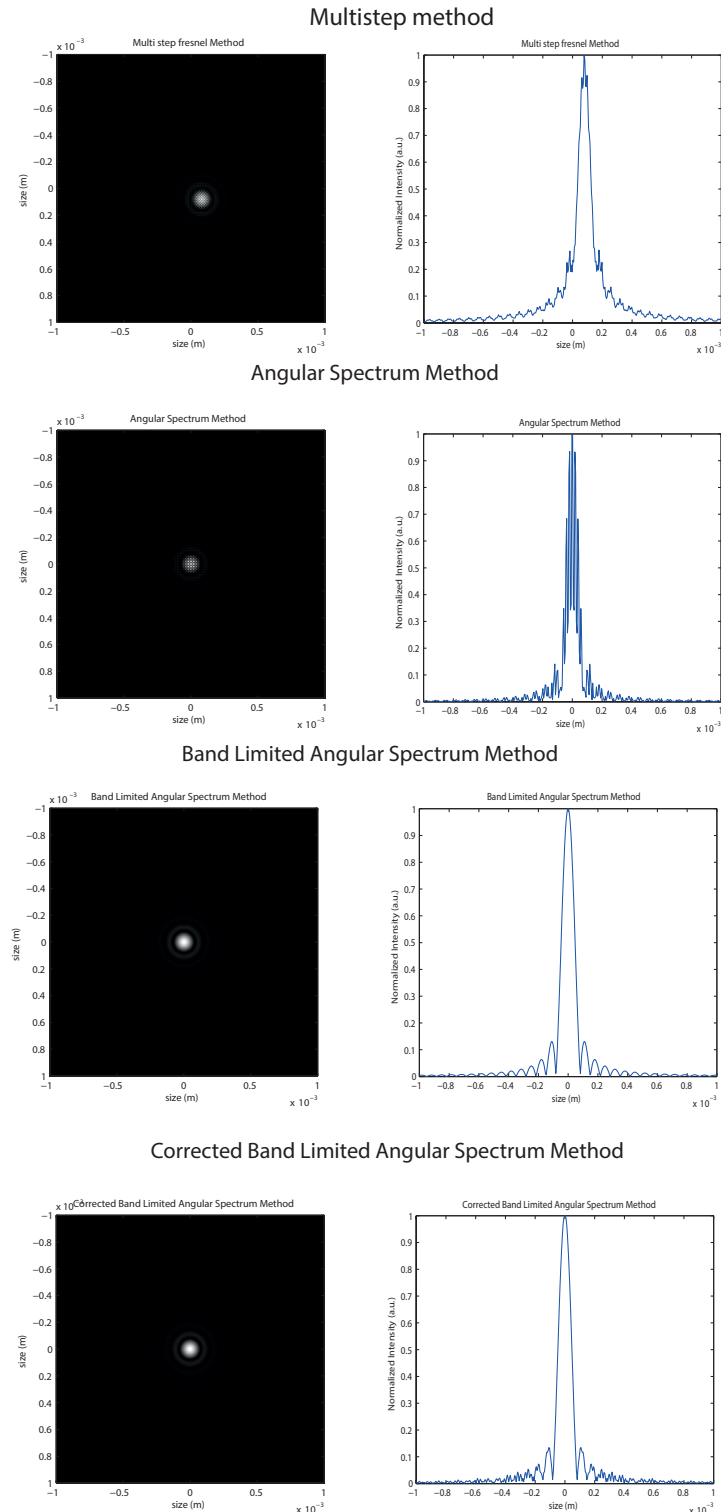


Figure 2.16: From top to Bottom: Image and intensity cross section of a point source according to multi step method, angular spectrum method, band limited angular spectrum method and corrected band limited angular spectrum method.

From figure 2.16 it can be seen that in the case of the Multi-step method the cross section of the impulse response does not go to zero because of additive background noise. The response of the angular spectrum method has a high frequency noise components superimposed to the diffraction pattern, while the band limited angular spectrum method reduces the noise due to aliasing of the transfer function in the angular spectrum case as can be seen comparing the two cross sections. Both the band limited and the corrected band limited methods present no background noise present in the multi step case and in the high frequency noise in the direct angular spectrum case. Another parameter to evaluate the accuracy of these methods is the position of the Airy disk first minimum. It is given by [47, 52]:

$$x_{min} = 1.22 \frac{\lambda z}{D} \quad (2.99)$$

where  $\lambda$  is the wavelength of the light propagating,  $D$  is the aperture of the lens and  $z$  the propagation distance. According to the values in section 2.6.1 the Airy disk should have its first minimum at  $x_{min} = 67\mu m$ . Without considering the multi step case that is too noisy and does not present zeros, the position of the first minimum is the other cases are:

AS	$67.5 \mu m$
BL	$77.5 \mu m$
cBL	$77.5 \mu m$

As expected for both the band limited angular spectrum the Airy Disk is slightly wider due to the low pass filtering action that transfer function has undergone. However noise is reduced sensibly with the band limitation. To better understand how the resolution changes with the different methods,

it is worth to have a look at the Fourier transform of the images shown in figure 2.16. The Fourier transform of the impulse response of a system give its frequency response. The shape of the frequency response gives information about how the frequencies components of the input signal are modulated and transferred to the output signal. When this function goes to zero the correspondent frequency value is called cutoff frequency. For frequencies higher than the cutoff frequency, all the information included in the input signal is lost. For the Results are shown in figure 2.17. The graphs are symmetric with respect to the zero frequency, therefore only the positive frequencies are shown.

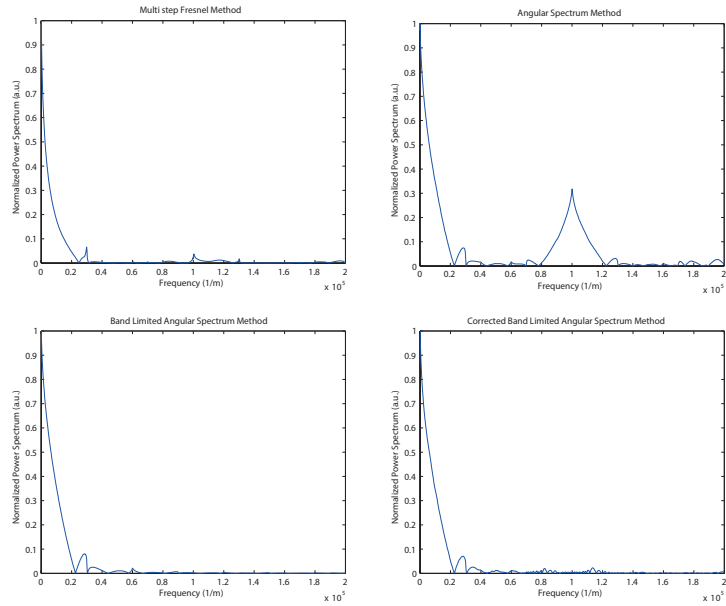


Figure 2.17: From top left to bottom right: Power spectrum of the image of a point source obtained with the multi step Fresnel method, the Angular spectrum method, the band limited angular spectrum method and the corrected band limited angular spectrum method .

From a comparison of the power spectra in figure 2.17 it is possible to note the difference in shape of the power spectrum of the multi step method, that goes to zero slower than the angular spectrum methods spectra. These three figures present as expected the same shape since for low frequency the three angular spectrum methods are identical, with the difference of the frequency components after the cutoff frequency due to the fact that the band limited and the corrected band limited have narrower bandwidths. In the Angular spectrum method graph it is present a strong peak at a frequency of  $10^5 \text{ } 1/m$  due to digital artefacts arisen from aliasing effects. this peak disappears in the other two band limited implementations of the angular spectrum.

## 2.7 Coherence

The Fresnel simulation toolbox has been designed to analyse a light field imaging system. The decision to develop an algorithm to simulate light propagating in a low state of coherence has been made in order too avoid interference pattern cross talk between neighbours lens lets that might decrease the quality of the final image. Diffraction, that is a deterministic property of light [53]. Once the characteristics of the input optical field are known, it is possible to use methods that allows to determine the characteristics of the output optical field completely such as the ones described in sections ??

Coherence is a statistical property of light and is described in terms of second order averages known as coherence function [53, 54]. A full analysis of coherence of optical fields can be found in text books such as Born and Wolf [55] and Goodman [53] and will not be discussed in this work. For the application described in this work coherence will be treated under a less rigorous point

of view, focusing on its practical effects on the optical experiments, and it will be used the physical causes of low coherent light in order to create a model to simulate different degrees of coherence. Before analysing the computational model of coherence it is worth to examine the two different types of coherence. As defined by Goodman [53] :

- **Temporal Coherence** can be defined as the ability of light to interfere with a delayed version of itself
- **Spatial Coherence** can be defined as the ability of light to interfere with a spatially shifted version of itself

The empirical method developed to simulate light propagating at low coherence includes both spatial and temporal coherence.

### 2.7.1 Temporal coherence

Following the explanation of Goodman [53], given a complex disturbance  $U(\vec{X}, t)$  with a finite bandwidth  $\Delta\nu$ , it is expected to remain constant during a time interval  $\tau < 1/\Delta\nu$ . This means that the disturbance taken at two different times in the same spatial position  $U(\vec{X}, t)$  and  $U(\vec{X}, t+\tau)$  are highly correlated if  $\tau < \tau_c$  where  $\tau_c$  is the coherence time. Since the correlation takes place without any spatial shift it is possible to drop the spatial coordinates  $\vec{X}$ . The degree of temporal coherence is therefore given by the autocorrelation function:

$$\Gamma(\tau) = \langle U(t + \tau)U^*(t) \rangle \quad (2.100)$$

The coherence time  $\tau$  is therefore a function of the bandwidth of the light. A perfectly monochromatic plane wave has a very narrow bandwidth and a

long time of coherence, while on the other hand ultra fast laser pulses will have a coherence time that is dependent by the bandwidth of the pulse. The shorter is the pulse, the broader the bandwidth. From the time of coherence it is possible to define the coherence length as  $l_c = v\tau_c$  where  $v = c/n$  is the speed of light in the medium of propagation given by the speed of light in the vacuum  $c$  divided by the refractive index  $n$ .

### 2.7.2 Spatial Coherence

To analyse spatial coherence two complex disturbances  $U(\vec{X}_1, t)$  and  $U(\vec{X}_2, t)$  are observed at the same time in two different position  $\vec{X}_1$  and  $\vec{X}_2$ . When the two points coincide,  $\vec{X}_1 = \vec{X}_2$  the two disturbances are perfectly correlated. When the distance between the two points begin to increase, the correlation degree decreases until they become totally uncorrelated. In order to better understand this concept it is useful to illustrate the Young experiment [56] [56]. With reference to figure 2.18 a squared light source of size  $\Delta x$  emits light towards a screen at a distance  $R$ . On the screen A there are two pinholes  $Q_1$  and  $Q_2$ . In order to have interference fringes on a second screen B the following condition should be satisfied:

$$\Delta x \Delta \theta < \lambda \quad (2.101)$$

Where  $2\theta$  is the angle formed at the source with the two pinholes  $Q_1$  and  $Q_2$  and  $\lambda$  is the wavelength of the light emitted by the source. In order to see the fringes, the two pinholes should be situated in an area  $\Delta A$  of size:

$$\Delta A \sim (R\Delta\theta)^2 = \frac{R^2}{S}\lambda \quad (2.102)$$

$R$  is the distance between the screen A and the source,  $S = \Delta x$  is the area of the source, and equation 2.101 has been used. The area  $\Delta A$  is the coherence area of the light in the plane A around the point  $Q_0$  on the optical axis.

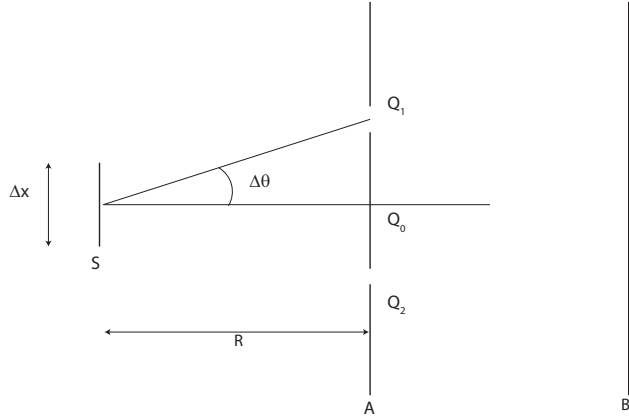


Figure 2.18: Young experiment setup.

The area of coherence quantifies the degree of spatial coherence. It depends on the area of the light source  $S$ , the distance of observation  $R$  and by the wavelength of the light. Interference fringes will be formed in the plane B more likely if the area of coherence is wide since the light remains correlated for even at a large distances  $z$ .

### 2.7.3 Simulation of spatial coherence

A novel method for simulating spatial coherence that generates a source optical field with a degree of coherence defined by the user. An electromagnetic wave is generated by a dipole oscillating at a certain frequency. This dipole can be a molecule, an atom, a group of atoms in a gas. In case of a conventional incandescence light source light is emitted by tungsten atoms exited by the electrical current. Same is valid for other sources of illuminations, like

gas lamps, neon, or solid state light sources like LED, atoms of molecules excited to higher energy level emit light when dropping on the ground energy level. Each dipole emits light with a certain initial phase. Considering a light source of surface  $\Sigma$ , containing oscillating dipoles, the elemental surfaces  $d\Sigma$  is defined as the surfaces on which all the dipoles oscillates with the same phase. The average dimension of the elemental surfaces  $d\Sigma$  is proportional to the degree of spatial coherence of the light source. The more coherent is the light source, the bigger the elemental surfaces will be. From a computational point of view having a light source composed by a mosaic of surfaces with different phases is equivalent to add a phase mask to the input field. This phase mask is composed by areas with a random phase value. The dimension of these areas gives an idea of the degree of spatial coherence. The idea behind the empirical method used to generate the phase mask is shown in figure 2.19:

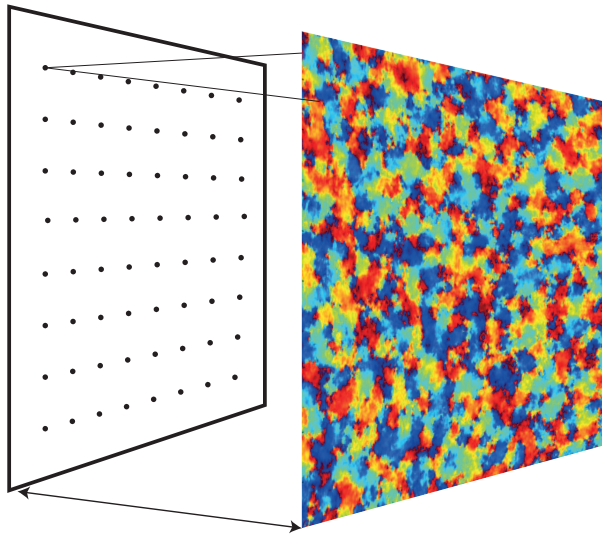


Figure 2.19: A random phase mask is generated propagating light coming from an array of sources, each one with a random phase value in the interval  $[-\pi, \pi]$ .

An array of point sources is displaced on a sampling window of the same dimension as the input field. The sources are placed regularly across the array. If the number of sources is less than 20, the sources are displaced randomly in order not to affect the coherence with their regular structure. The number of point sources used is defined as the coherence index  $C$ . To each of these point sources is assigned a random value of phase in the range  $[-\pi, \pi]$  and an amplitude value of one. Then the array of point sources is convolved with a kernel  $K$  whose size is defined in order to make all the random point sources to merge together. The size of the kernel depends on the resolution  $N$  of the input field and on the coherence index  $C$  and is equal to the ratio  $N/C$ . The result of the convolution is a phase mask that is formed by an array of circular areas with a random phase value. Although this array of sources is already a phase mask, it cannot be used into the

simulation platform, because of its periodicity. In fact it is not a random phase pattern. In order to randomize the shape and the distribution of the coherence areas the array of sources is propagated at a distance bigger than the size of the sources. The distance chosen to propagate the light sources is the one derived in 2.3.1 to keep the same sampling both in the input and output fields using the Fresnel propagation method discussed in section.

From equation 2.34:

$$d_c = \frac{W^2}{N\lambda} \quad (2.103)$$

where  $W$  is the field of view,  $N$  is the sampling and  $\lambda$  is the wavelength of the light. The choice of using the Fresnel propagation as described in section 2.3 has been made because the propagation distance is small and hence aliasing issues do not arise. In addition to that it only requires one Fourier transform, making the random phase generation algorithm faster. The whole process is shown in figure 2.20

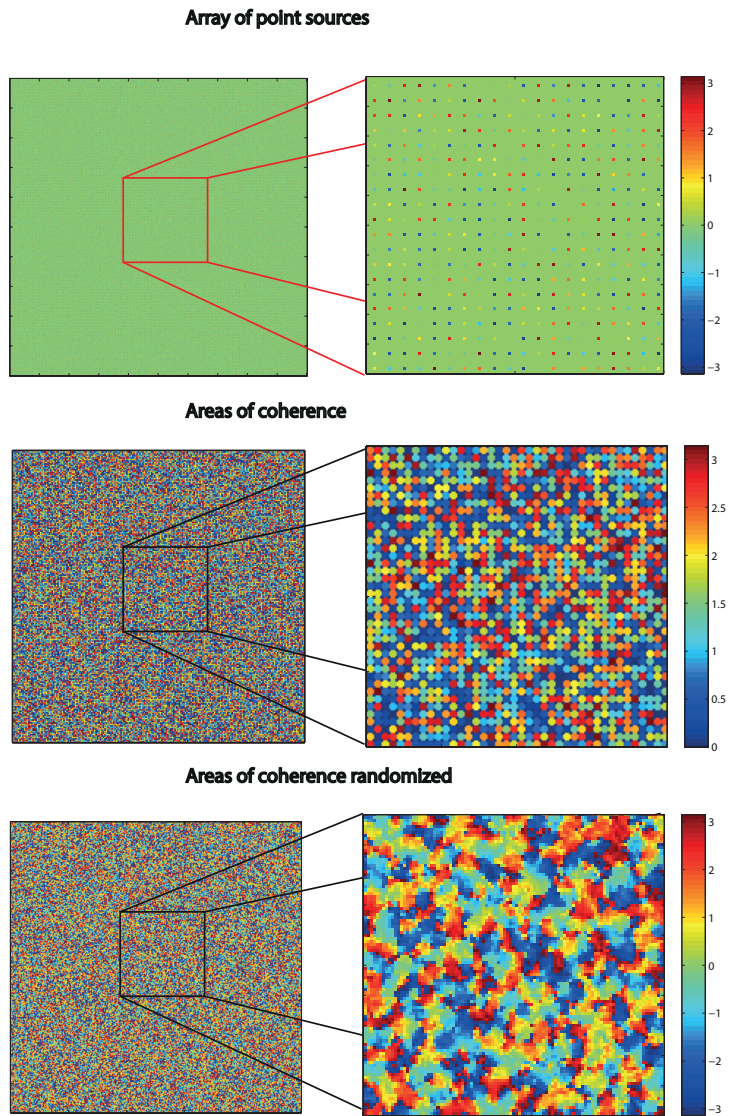


Figure 2.20: Process of the creation of the phase mask. Top: array of point sources with a random phase value; centre: array of the areas of coherence at source after the convolution with  $K$ ; bottom: randomized areas of coherence at object plane after the propagation of  $d_c$ .

Few examples of phase mask generated from different number of sources can be seen in figure 2.21:

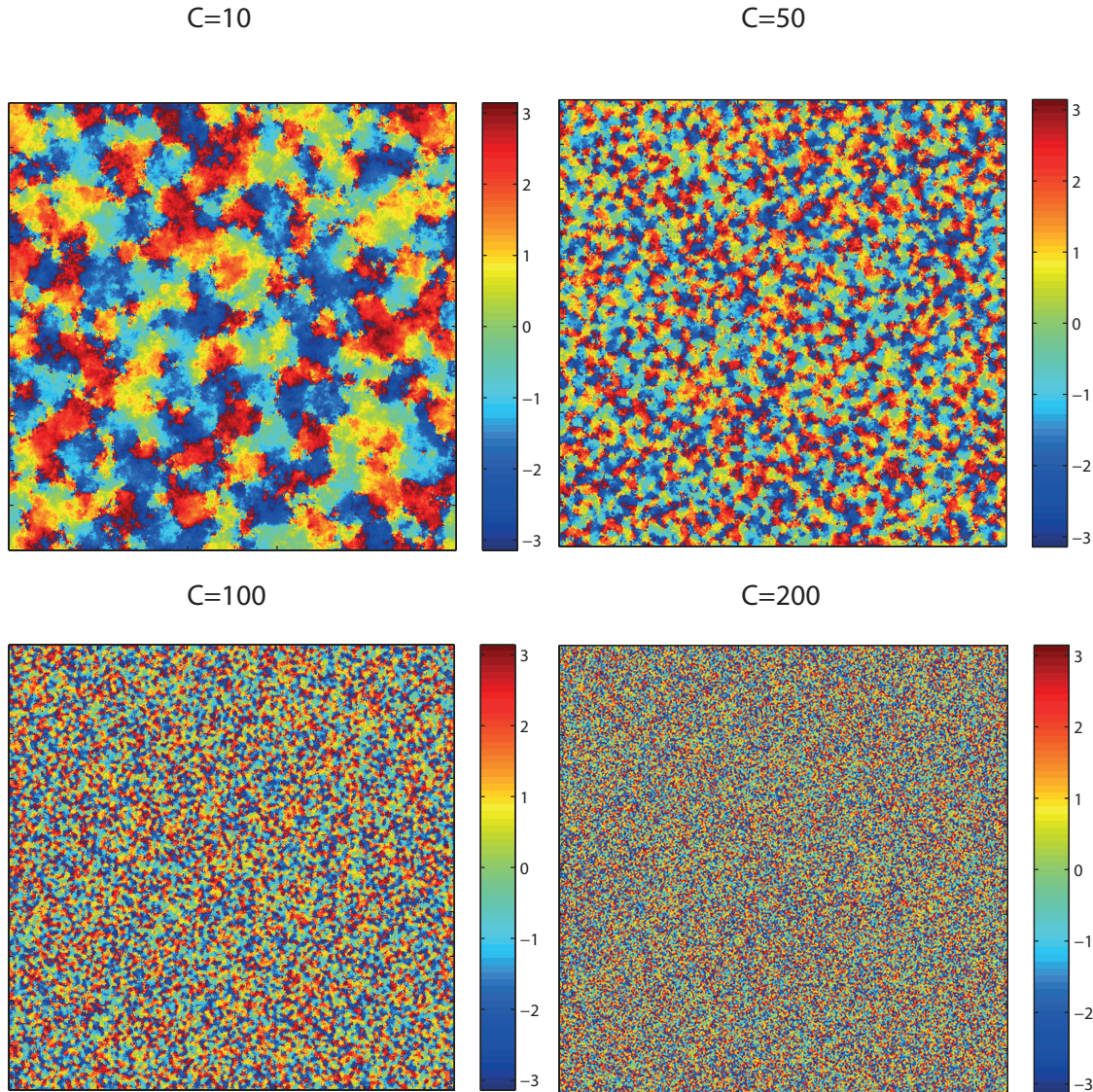


Figure 2.21: Final random phase mask generated by 10, 50, 100 and 200 sources.

The algorithm to generate the random phase mask can be summarized as follow:

- A number of light sources, are defined and arranged in a regular array, and allocated a random phase between  $-\pi$  and  $\pi$ .

- Each source has a size diameter given by:  $N/C$
  
  
  
  
  
  
- This array of sources is then propagated a distance  $d_c$  shown in equation 2.103 in order to randomize the shape of the coherence areas.
  
  
  
  
  
  
- the resultant phase is used as the output phase mask to add the input field.

#### 2.7.4 Simulation of temporal coherence

As discussed in section 2.7.1, temporal coherence is defined by the time  $\tau$  in which the optical wave is correlated with itself. In other words after a time  $t = \tau$ , the optical disturbance  $U(t)$  and  $U(t + \tau)$  are totally uncorrelated and cannot interfere with each other. To simulate this effect many snapshots of the output field are taken each time using a different random distribution phases for the sources. We assume that the time difference between every snapshots is equal to the coherence time  $\tau$ . For the application for which this toolbox has been designed it is not relevant to know the exact value of  $\tau$ . However, the light source used for the real system was a "Thorlabs LED Array Light Source LIU630A", with a wavelength centred on 630 nm and a bandwidth  $\Delta\lambda = 20nm$ . The emission spectrum is shown in figure 2.22.

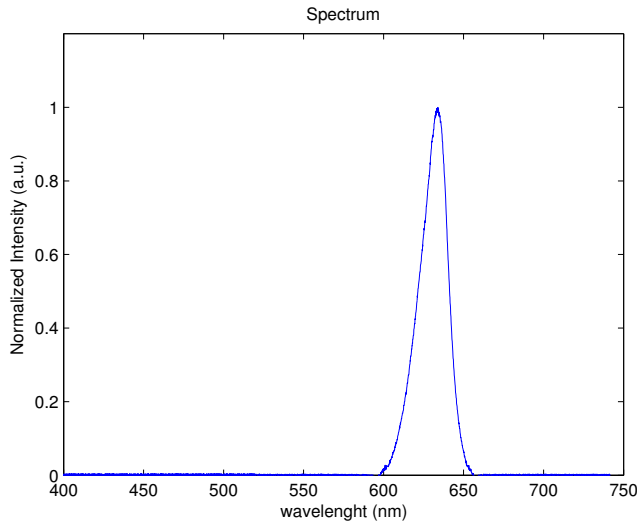


Figure 2.22: Emission spectrum of the LED considered in our simulations and real image system.

Its coherence time is given by:

$$\tau = \frac{1}{\Delta\nu} = \frac{\Delta\lambda}{c} \quad (2.104)$$

That gives a time of coherence  $\tau = 6.6 \times 10^{-17}s$ . Therefore each snapshot is assumed to be taken at the image plane at an interval of  $\tau$ . All the snapshots are then added together, integrating the optical disturbance over time. Longer integration times will give better contrast and less noise as it is shown in the following paragraph.

## 2.8 Optimization of coherence parameters

In the previous sections has been described how to simulate partially coherent light and how to implement an algorithm that produces a certain number of snapshots of the output field each one with a different random phase. The

random phase mask simulates the spatial coherence, the number of iteration instead simulates the effects of temporal coherence.

### 2.8.1 Optimization of Spatial Coherence

In this section will be defined the optimal value of coherence degree  $C$  and evaluating the signal to noise ratio of the outcome images from the 2f system shown in figure 2.14. Simulations have been run propagating an optical disturbance with phase masks generated with different values of the parameter  $C$ . The input field is the USAF resolution target, shown in 2.23

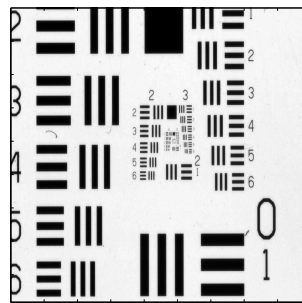


Figure 2.23: USAF resolution target.

The first simulation has been made changing the coherence index  $C$  from a value of 5 (high coherence) to 500 (low coherence) in a sampling window with a resolution of 1765 by 1765 pixels. Figure 2.25 shows how the field at the image plane for different values of  $C$  appears, while figure 2.24 shows a plot of the signal to noise ratio of the images as a function of the coherence index showing an asymptotic behaviour. After a certain threshold value of  $C$ , increasing the coherence index does not improve the image quality. The threshold is defined as the value of  $C$  for which the variance of the previous five values of SNR is less than 0.01.

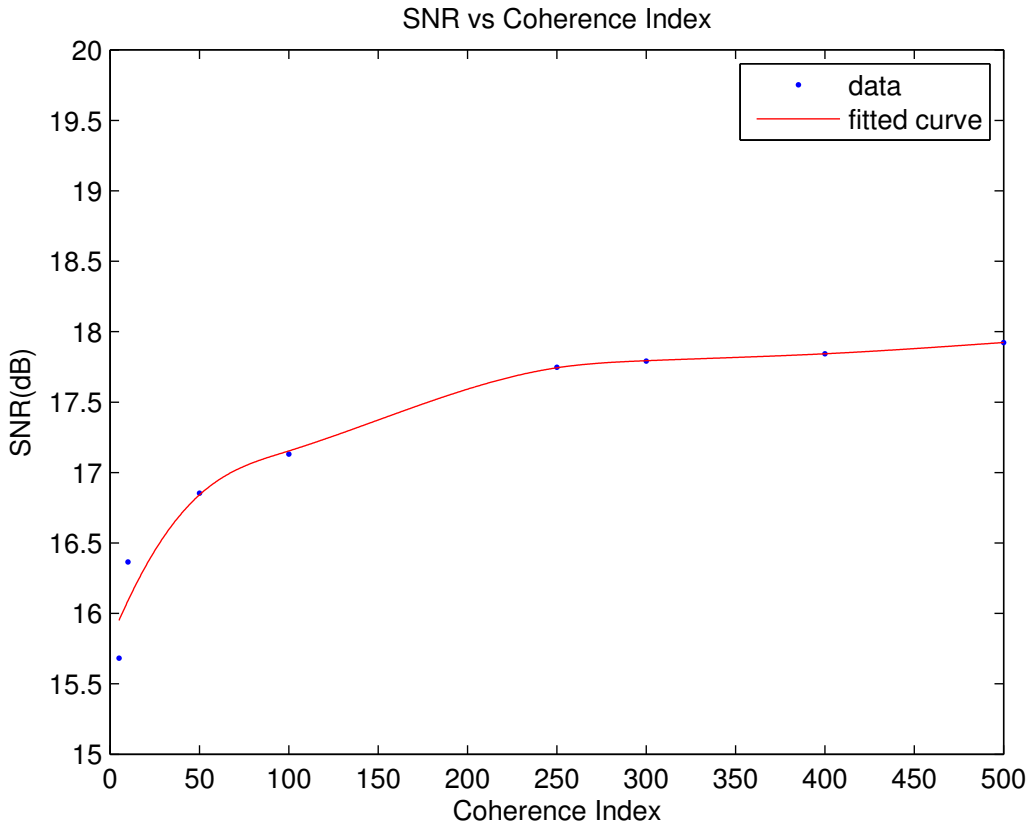


Figure 2.24: Signal to noise ratio of the image of a USAF resolution target plotted as a function of the coherence index  $C$ .

Figure 2.24 shows that for values of  $C$  bigger than 250 the SNR asymptotically tends to 18. In this case the resolution of the input field, and therefore of the phase mask, is 1765 by 1765 pixels, so that the SNR reaches the asymptote when the ratio between the number of sources and the resolution should be 0.14. After this point, there is no gain in making the light source more incoherent in terms of signal to noise ratio improvement. The ratio between the number of sources  $C$  and the resolution of the optical field  $N$  is defined as the incoherence degree  $\iota$ :

$$\iota = \frac{C}{N} \quad (2.105)$$

In figure 2.25 are shown the images of the target shown in 2.23 obtained with different incoherence parameters  $\iota$

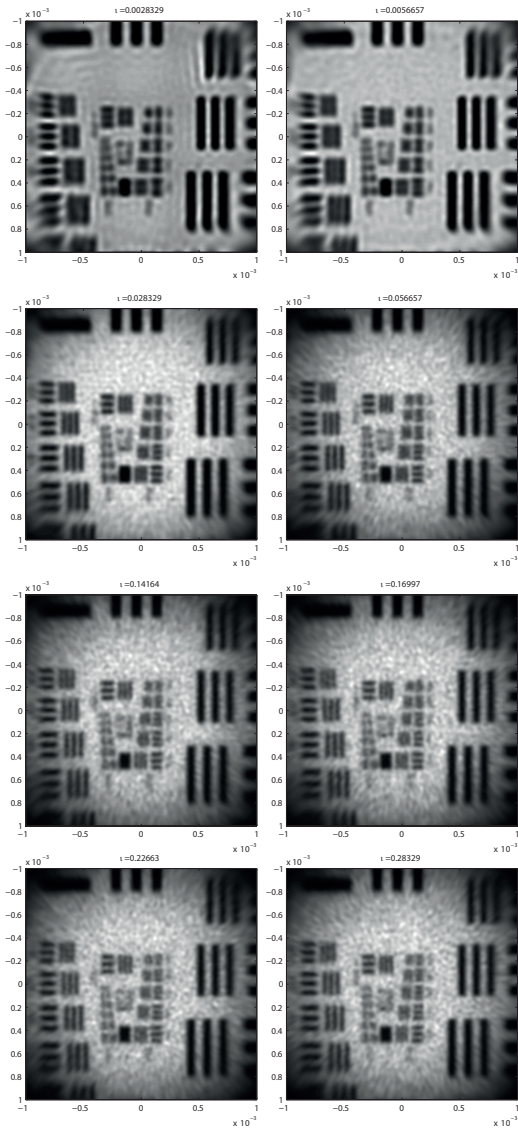


Figure 2.25: Images of the USAF resolution target with different values of  $\iota$ . Increasing the number of point sources generating the phase mask creates improves the resolution and the contrast

### 2.8.2 Optimization of temporal coherence

The second simulation run aimed to define the optimum number of snapshots in order to correctly simulate temporal coherence. The random phase mask acts as a diffuser, and the resultant output field obtained by a single snapshot will present a low signal to noise ratio due to speckles, as shown in figure 2.26

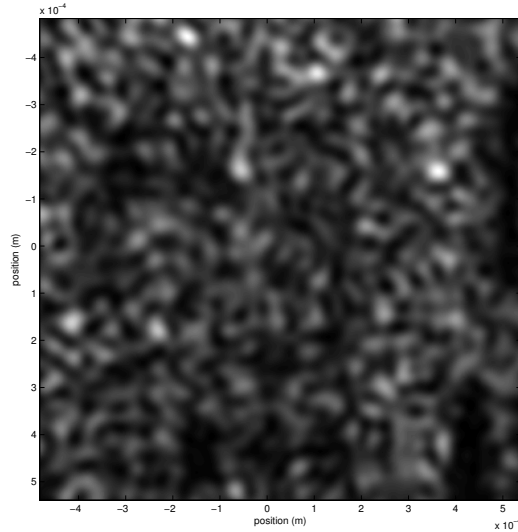


Figure 2.26: Noise due to the speckles in an image of a USAF resolution target after only 5 iterations.

Taking several snapshots and adding them all together is equal to integration over time of the optical field reaching the sensor. While increasing the integration time, the noise due to the speckles drops considerably. Figure 2.27 shows several images of the USAF target in figure 2.23 taken with an incoherence degree of  $\iota = 0.14$ , and with an increasing number of iterations from 5 to 1000.



Figure 2.27: Images of the USAF resolution target obtained adding an increasing number of snapshot. this is equivalent to increase the integration time of the sensor. The noise due to the speckles caused by the phase mask decreases with increasing number of iterations.

Since increasing the number of iterations is computationally expensive, the signal to noise ratio of the images in figure 2.27 has been evaluated and plotted as a function of the number of iteration in order to define an optimal parameter. Results are shown in figure 2.28. The threshold is defined as the number of iterations for which the variance of the previous five values of SNR is less than 0.01.

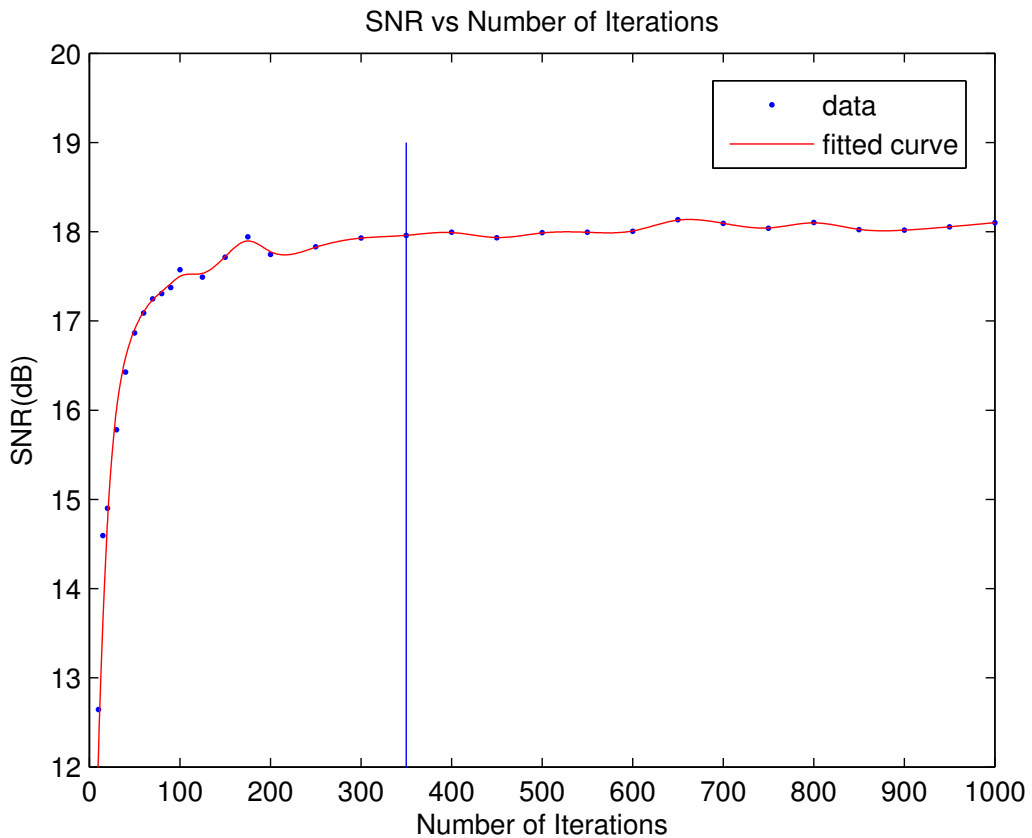


Figure 2.28: Signal to noise ratio as a function of the number of iterations. The threshold has been calculated looking at the variance of the previous five data.

For an image with an incoherence degree of  $\iota = 0.14$  the minimum number of iterations after that the SNR of the image does not improve further is

350. After that value the SNR tends asymptotically to 18 dB in spite of an increased computational effort. Therefore under a SNR point of view the optimal number of iteration to simulate temporal incoherence is 350. All the other simulations presented in this work will be performed with the coherence parameters discussed in this section.

### 2.8.3 Coherent imaging vs incoherent imaging

The image of an edge has been simulated to make a comparison between the coherent and the incoherent response. Data were simulated with the same optical parameters described in section 2.6.1. The intensity profile of an image of an edge is well known both in the case of coherent and incoherent illumination and provides a means of verification for the simulation methodology discussed above. Figure 2.29 shows the response of a coherent and an incoherent imaging systems to a sharp edge. The intensity profile of the edge is shown in green, its coherent image in blue and the incoherent image is shown in red. The two responses are very different. The coherent image presents fringes whose amplitude goes decreasing getting further away from the edge. This effect is known as ringing artefacts, due to the coherent transfer function that usually presents rapid discontinuities [47]. Another property of the coherent image is that it crosses the actual location of the edge at  $1/4$  of its asymptotic value of intensity, while the incoherent image does the same at  $1/2$  of its asymptotic value, as can be seen in figure 2.29 [47]. Both conditions are verified by the simulations run as shown in figure 2.29.

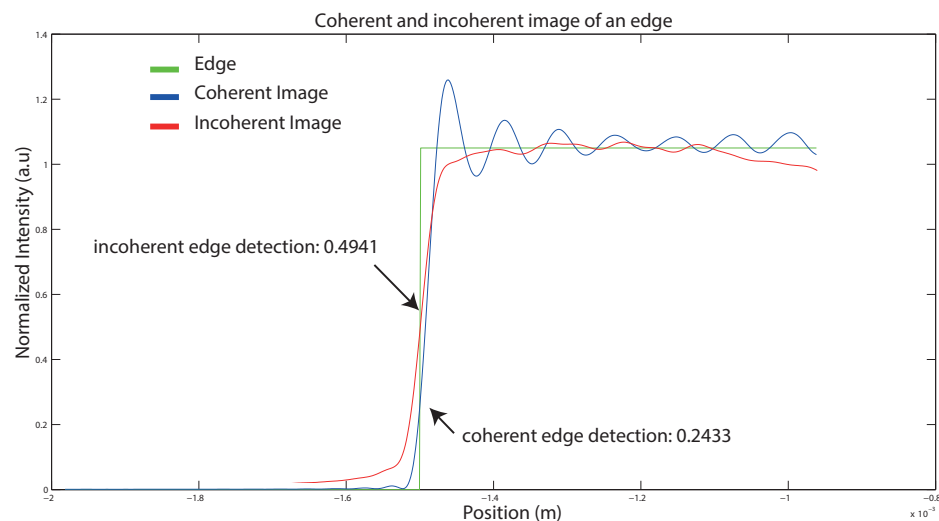


Figure 2.29: Comparison between the coherent and an incoherent response of a simple 2f system to a sharp edge.



# Bibliography

- [1] Shree K Nayar. Computational cameras: Redefining the image. *Computer*, (8):30–38, 2006.
- [2] Ren Ng. *Digital light field photography*. PhD thesis, stanford university, 2006.
- [3] Todor Georgiev and Andrew Lumsdaine. Focused plenoptic camera and rendering. *Journal of Electronic Imaging*, 19(2):021106–021106, 2010.
- [4] Levoy Mark. Stanford light field microscope project, 2005.
- [5] Joseph Carroll, David B Kay, Drew Scoles, Alfredo Dubra, and Marco Lombardo. Adaptive optics retinal imaging-clinical opportunities and challenges. *Current eye research*, 38(7):709–721, 2013.
- [6] Gordon Wetzstein, Ivo Ihrke, Douglas Lanman, and Wolfgang Heidrich. Computational plenoptic imaging. In *Computer Graphics Forum*, volume 30, pages 2397–2426. Wiley Online Library, 2011.
- [7] Edward H Adelson and James R Bergen. *The plenoptic function and the elements of early vision*. Vision and Modeling Group, Media Laboratory, Massachusetts Institute of Technology, 1991.

- [8] Edward H Adelson and John Y. A. Wang. Single lens stereo with a plenoptic camera. *IEEE Transactions on Pattern Analysis & Machine Intelligence*, (2):99–106, 1992.
- [9] Plato and Francis Macdonald Cornford. *The republic of Plato*, volume 30. Oxford University Press New York, 1945.
- [10] Herbert E Ives. Parallax panoramagrams made with a large diameter lens. *J. Opt. Soc. Amer*, 20:332–342, 1930.
- [11] Frederic E Ives. Parallax stereogram and process of making same., April 14 1903. US Patent 725,567.
- [12] Lippmann Gabriel. La photographie intégrale. *Comptes-Rendus, Académie des Sciences*, 146:446–551, 1908.
- [13] Marc Levoy and Pat Hanrahan. Light field rendering. In *Proceedings of the 23rd annual conference on Computer graphics and interactive techniques*, pages 31–42. ACM, 1996.
- [14] Yuichi Taguchi, Amit Agrawal, Srikumar Ramalingam, and Ashok Veeraraghavan. Axial light field for curved mirrors: Reflect your perspective, widen your view. In *Computer Vision and Pattern Recognition (CVPR), 2010 IEEE Conference on*, pages 499–506. IEEE, 2010.
- [15] Steven J Gortler, Radek Grzeszczuk, Richard Szeliski, and Michael F Cohen. The lumigraph. In *Proceedings of the 23rd annual conference on Computer graphics and interactive techniques*, pages 43–54. ACM, 1996.

- [16] Bennett S Wilburn, Michal Smulski, Hsiao-Heng K Lee, and Mark A Horowitz. Light field video camera. In *Electronic Imaging 2002*, pages 29–36. International Society for Optics and Photonics, 2001.
- [17] Jason C Yang, Matthew Everett, Chris Buehler, and Leonard McMillan. A real-time distributed light field camera. *Rendering Techniques*, 2002:77–86, 2002.
- [18] Yoshikuni Nomura, Li Zhang, and Shree K Nayar. Scene collages and flexible camera arrays. In *Proceedings of the 18th Eurographics conference on Rendering Techniques*, pages 127–138. Eurographics Association, 2007.
- [19] Todor Georgiev, Ke Colin Zheng, Brian Curless, David Salesin, Shree Nayar, and Chintan Intwala. Spatio-angular resolution tradeoffs in integral photography. *Rendering Techniques*, 2006:263–272, 2006.
- [20] Massimo Turola and Steve Gruppetta. Wave optics simulations of a focused plenoptic system. In *Frontiers in Optics*, pages JTU3A–24. Optical Society of America, 2014.
- [21] Ren Ng, Marc Levoy, Mathieu Brédif, Gene Duval, Mark Horowitz, and Pat Hanrahan. Light field photography with a hand-held plenoptic camera. *Computer Science Technical Report CSTR*, 2(11), 2005.
- [22] Kensuke Ueda, Takafumi Koike, Keita Takahashi, and Takeshi Naemura. Adaptive integral photography imaging with variable-focus lens array. In *Electronic Imaging 2008*, pages 68031A–68031A. International Society for Optics and Photonics, 2008.

- [23] Ashok Veeraraghavan, Ramesh Raskar, Amit Agrawal, Ankit Mohan, and Jack Tumblin. Dappled photography: Mask enhanced cameras for heterodyned light fields and coded aperture refocusing. *ACM Trans. Graph.*, 26(3):69, 2007.
- [24] Douglas Lanman, Ramesh Raskar, Amit Agrawal, and Gabriel Taubin. Shield fields: modeling and capturing 3d occluders. *ACM Transactions on Graphics (TOG)*, 27(5):131, 2008.
- [25] Kshitij Marwah, Gordon Wetzstein, Yosuke Bando, and Ramesh Raskar. Compressive light field photography using overcomplete dictionaries and optimized projections. *ACM Transactions on Graphics (TOG)*, 32(4):46, 2013.
- [26] Yu Ji, Jinwei Ye, and Jingyi Yu. Depth reconstruction from the defocus effect of an xslit camera. In *Computational Optical Sensing and Imaging*, pages CM4E–3. Optical Society of America, 2015.
- [27] Todor Georgiev and Andrew Lumsdaine. The multifocus plenoptic camera. In *IS&T/SPIE Electronic Imaging*, pages 829908–829908. International Society for Optics and Photonics, 2012.
- [28] Todor Georgiev and Chintan Intwala. Light field camera design for integral view photography. *Adobe System, Inc*, 2006.
- [29] Tom E Bishop, Sara Zanetti, and Paolo Favaro. Light field superresolution. In *Computational Photography (ICCP), 2009 IEEE International Conference on*, pages 1–9. IEEE, 2009.

- [30] Sapna A Shroff and Kathrin Berkner. Image formation analysis and high resolution image reconstruction for plenoptic imaging systems. *Applied optics*, 52(10):D22–D31, 2013.
- [31] Todor Georgiev and Andrew Lumsdaine. Superresolution with plenoptic camera 2.0. *Adobe Systems Incorporated, Tech. Rep*, 2009.
- [32] Todor Georgiev. Plenoptic camera resolution. In *Computational Optical Sensing and Imaging*, pages JTh4A–2. Optical Society of America, 2015.
- [33] Changyin Zhou and Shree K Nayar. Computational cameras: Convergence of optics and processing. *Image Processing, IEEE Transactions on*, 20(12):3322–3340, 2011.
- [34] Andrew Lumsdaine and Todor Georgiev. Full resolution lightfield rendering. *Indiana University and Adobe Systems, Tech. Rep*, 2008.
- [35] Andrew Lumsdaine and Todor Georgiev. The focused plenoptic camera. In *Computational Photography (ICCP), 2009 IEEE International Conference on*, pages 1–8. IEEE, 2009.
- [36] Tom E Bishop and Paolo Favaro. Full-resolution depth map estimation from an aliased plenoptic light field. In *Computer Vision–ACCV 2010*, pages 186–200. Springer, 2011.
- [37] Todor G Georgiev and Andrew Lumsdaine. Resolution in plenoptic cameras. In *Computational Optical Sensing and Imaging*, page CTuB3. Optical Society of America, 2009.

- [38] Victor Guillemin and Shlomo Sternberg. *Symplectic techniques in physics*. Cambridge University Press, 1990.
- [39] Todor Georgiev, Andrew Lumsdaine, and Sergio Goma. Plenoptic principal planes. In *Imaging Systems and Applications*, page JTuD3. Optical Society of America, 2011.
- [40] Sapna Shroff and Kathrin Berkner. High resolution image reconstruction for plenoptic imaging systems using system response. In *Computational Optical Sensing and Imaging*, pages CM2B–2. Optical Society of America, 2012.
- [41] Gabriel C Birch, J Scott Tyo, and Jim Schwiegerling. Depth measurements through controlled aberrations of projected patterns. *Optics express*, 20(6):6561–6574, 2012.
- [42] Joyce E Farrell, Peter B Catrysse, and Brian A Wandell. Digital camera simulation. *Applied Optics*, 51(4):A80–A90, 2012.
- [43] Brian S Thurow and Timothy Fahringer. Recent development of volumetric piv with a plenoptic camera. In *PIV13; 10th International Symposium on Particle Image Velocimetry, Delft, The Netherlands, July 1-3, 2013*. Delft University of Technology, Faculty of Mechanical, Maritime and Materials Engineering, and Faculty of Aerospace Engineering, 2013.
- [44] Kyle Lynch. *Development of a 3-D fluid velocimetry technique based on light field imaging*. PhD thesis, Auburn University, 2011.

- [45] Kyle Lynch, Tim Fahringer, and Brian Thurow. Three-dimensional particle image velocimetry using a plenoptic camera. In *AIAA Aerospace Sciences Meeting*, 2012.
- [46] Arnold Sommerfeld. Optics lectures on theoretical physics, vol. iv. *Optics Lectures on Theoretical Physics, Vol. IV by Arnold Sommerfeld* New York, NY: Academic Press INC, 1954, 1, 1954.
- [47] Joseph W Goodman. *Introduction to Fourier optics*. Roberts and Company Publishers, 2005.
- [48] Maciej Sypek. Light propagation in the fresnel region. new numerical approach. *Optics communications*, 116(1):43–48, 1995.
- [49] Rafael C Gonzalez, Richard Eugene Woods, and Steven L Eddins. *Digital image processing using MATLAB*. Pearson Education India, 2004.
- [50] Kyoji Matsushima and Tomoyoshi Shimobaba. Band-limited angular spectrum method for numerical simulation of free-space propagation in far and near fields. *Optics express*, 17(22):19662–19673, 2009.
- [51] Maciej Sypek. Reply to the comment on “light propagation in the fresnel region–new numerical approach”. *Optics Communications*, 282(6):1074–1077, 2009.
- [52] Frank L Pedrotti and Leno S Pedrotti. Introduction to optics 2nd edition. *Introduction to Optics 2nd Edition by Frank L. Pedrotti, SJ, Leno S. Pedrotti* New Jersey: Prentice Hall, 1993, 1, 1993.

- [53] Joseph W Goodman and Randy L Haupt. *Statistical optics*. John Wiley & Sons, 2015.
- [54] Leonard Mandel and Emil Wolf. *Optical coherence and quantum optics*. Cambridge university press, 1995.
- [55] Max Born and Emil Wolf. *Principles of optics: electromagnetic theory of propagation, interference and diffraction of light*. Cambridge university press, 1999.
- [56] Emil Wolf. *Introduction to the Theory of Coherence and Polarization of Light*. Cambridge University Press, 2007.
- [57] Todor G Georgiev and Andrew Lumsdaine. Super-resolution with the focused plenoptic camera, November 20 2012. US Patent 8,315,476.
- [58] Christian Perwass and Lennart Wietzke. Single lens 3d-camera with extended depth-of-field. In *Proc. SPIE*, volume 8291, page 829108, 2012.
- [59] Michael Hansen and Eric Holk. Depth map estimation for plenoptic images. 2011.
- [60] Ole Johannsen, Christian Heinze, Bastian Goldluecke, and Christian Perwass. On the calibration of focused plenoptic cameras. In *Time-of-Flight and Depth Imaging. Sensors, Algorithms, and Applications*, pages 302–317. Springer, 2013.
- [61] Hans Peter Herzig. *Micro-optics: elements, systems and applications*. CRC Press, 1997.

- [62] Todor Georgiev, Georgi Chunev, and Andrew Lumsdaine. Superresolution with the focused plenoptic camera. In *IS&T/SPIE Electronic Imaging*, pages 78730X–78730X. International Society for Optics and Photonics, 2011.
- [63] Todor G Georgiev, Andrew Lumsdaine, and Sergio Goma. High dynamic range image capture with plenoptic 2.0 camera. In *Signal recovery and synthesis*, page SWA7P. Optical Society of America, 2009.
- [64] Paolo Favaro. A split-sensor light field camera for extended depth of field and superresolution. In *SPIE Photonics Europe*, pages 843602–843602. International Society for Optics and Photonics, 2012.
- [65] Tom E Bishop and Paolo Favaro. The light field camera: Extended depth of field, aliasing, and superresolution. *Pattern Analysis and Machine Intelligence, IEEE Transactions on*, 34(5):972–986, 2012.
- [66] Chien-Hung Lu, Stefan Muenzel, and Jason Fleischer. High-resolution light-field microscopy. In *Computational Optical Sensing and Imaging*, pages CTh3B–2. Optical Society of America, 2013.
- [67] Vivek Boominathan, Kaushik Mitra, and Ashok Veeraraghavan. Improving resolution and depth-of-field of light field cameras using a hybrid imaging system. In *Computational Photography (ICCP), 2014 IEEE International Conference on*, pages 1–10. IEEE, 2014.
- [68] Photonics for Innovations Quioptiq. *The Linos Catalog*. 2015.

- [69] August Köhler. A new system of illumination for photomicrographic purposes. *Z. Wiss. Mikroskopie*, 10:433–440, 1893.
- [70] August Kohler and Walter Bauersfeld. Device for light-field and dark-field illumination of microscopic objects, January 16 1934. US Patent 1,943,510.